



REVISED MASSES AND DENSITIES OF THE PLANETS AROUND KEPLER-10*

LAUREN M. WEISS^{1,9}, LESLIE A. ROGERS^{2,10}, HOWARD T. ISAACSON¹, ERIC AGOL^{3,4}, GEOFFREY W. MARCY¹, JASON F. ROWE⁵,
DAVID KIPPING⁶, BENJAMIN J. FULTON⁷, JACK J. LISSAUER⁵, ANDREW W. HOWARD⁷, AND DANIEL FABRYCKY⁸

¹Astronomy Department, University of California at Berkeley, 501 Campbell Hall, Berkeley, CA 94720, USA; lweiss@berkeley.edu

²California Institute of Technology Division of Geological and Planetary Sciences, 1200 East California Boulevard, Pasadena, CA 91125, USA

³NASA Astrobiology Institute's Virtual Planetary Laboratory, Pasadena, CA 91125, USA

⁴Department of Astronomy, University of Washington, Box 351580, Seattle, WA 98195, USA

⁵NASA Ames Research Center, Moffett Field, CA 94035, USA

⁶Harvard University Center for Astrophysics, 60 Garden Street, Cambridge, MA 02138, USA

⁷Institute for Astronomy, University of Hawaii at Manoa, Honolulu, HI 96822, USA

⁸Department of Astronomy and Astrophysics, The University of Chicago, 5640 South Ellis Avenue, Chicago, IL 60637, USA

Received 2015 August 12; accepted 2016 January 20; published 2016 March 1

ABSTRACT

Determining which small exoplanets have stony-iron compositions is necessary for quantifying the occurrence of such planets and for understanding the physics of planet formation. Kepler-10 hosts the stony-iron world Kepler-10b, and also contains what has been reported to be the largest solid silicate-ice planet, Kepler-10c. Using 220 radial velocities (RVs), including 72 precise RVs from Keck-HIRES of which 20 are new from 2014 to 2015, and 17 quarters of *Kepler* photometry, we obtain the most complete picture of the Kepler-10 system to date. We find that Kepler-10b ($R_p = 1.47 R_\oplus$) has mass $3.72 \pm 0.42 M_\oplus$ and density $6.46 \pm 0.73 \text{ g cm}^{-3}$. Modeling the interior of Kepler-10b as an iron core overlaid with a silicate mantle, we find that the iron core constitutes 0.17 ± 0.11 of the planet mass. For Kepler-10c ($R_p = 2.35 R_\oplus$) we measure mass $13.98 \pm 1.79 M_\oplus$ and density $5.94 \pm 0.76 \text{ g cm}^{-3}$, significantly lower than the mass computed in Dumusque et al. ($17.2 \pm 1.9 M_\oplus$). Our mass measurement of Kepler-10c rules out a pure stony-iron composition. Internal compositional modeling reveals that at least 10% of the radius of Kepler-10c is a volatile envelope composed of hydrogen–helium (0.2% of the mass, 16% of the radius) or super-ionic water (28% of the mass, 29% of the radius). However, we note that analysis of only HIRES data yields a higher mass for planet b and a lower mass for planet c than does analysis of the HARPS-N data alone, with the mass estimates for Kepler-10 c being formally inconsistent at the 3σ level. Moreover, dividing the data for each instrument into two parts also leads to somewhat inconsistent measurements for the mass of planet c derived from each observatory. Together, this suggests that time-correlated noise is present and that the uncertainties in the masses of the planets (especially planet c) likely exceed our formal estimates. Transit timing variations (TTVs) of Kepler-10c indicate the likely presence of a third planet in the system, KOI-72.X. The TTVs and RVs are consistent with KOI-72.X having an orbital period of 24, 71, or 101 days, and a mass from 1 to $7 M_\oplus$.

Key words: planetary systems – planets and satellites: composition – planets and satellites: detection – planets and satellites: fundamental parameters – planets and satellites: terrestrial planets – techniques: radial velocities

1. INTRODUCTION

The thousands of high-fidelity planet candidates between 1 and 4 Earth radii discovered by the *Kepler* Mission (Borucki et al. 2011; Batalha et al. 2013; Burke et al. 2014; Rowe et al. 2014; Mullally et al. 2015), though absent from our solar system, are abundant in orbital periods < 100 days around Sun-like stars (Fressin et al. 2013; Petigura et al. 2013a, 2013b). To understand the formation of these common planets, we must constrain their compositions. Are they terrestrial, or are they “water worlds” that are primarily water by volume, or are they stony-iron cores overlaid with thick, hydrogen-rich envelopes of volatiles?

In the last few years, the exoplanet community has measured the masses of dozens of small exoplanets, enabling the study of the compositions of individual planets and the identification of several stony-iron super-Earths. Corot-7 b ($R_p = 1.58 \pm 0.10 R_\oplus$, $M_p = 5.37 \pm 1.02 M_\oplus$; Bruntt et al. 2010; Haywood et al. 2014) and Kepler-10 b ($R_p =$

$1.46 \pm 0.034 R_\oplus$, $M_p = 4.56 \pm 1.23 M_\oplus$; Batalha et al. 2011) were the first stony-iron planets discovered. Carter et al. (2012) used transit timing variations (TTVs) to determine the mass of Kepler-36 b from orbital perturbations it induced on neighboring planet Kepler-36 c. At the time of writing, Kepler-36 b has the best-determined mass and density of the known rocky exoplanets ($M_p = 4.56 \pm 1.23$, $\rho_p = 8.8 \pm 2.5 \text{ g cm}^{-3}$). Howard et al. (2013), Pepe et al. (2013), and Grunblatt et al. (2015) measured the mass of the Earth-density planet Kepler-78 b ($R_p = 1.20 \pm 0.09 R_\oplus$, $M_p = 1.87 \pm 0.26 M_\oplus$, $\rho_p = 6.0 \pm 1.7 \text{ g cm}^{-3}$), the closest Earth-analog in terms of planet mass, radius, and density, although it is far too hot to support life as we know it.

However, some small planets have definitively non-rocky surfaces and require hydrogen–helium envelopes to explain their low bulk densities. For instance, three of the six planets orbiting Kepler-11 are smaller than $4 R_\oplus$ and have densities lower than 1.0 g cm^{-3} (Lissauer et al. 2011, 2013). Likewise, two of four the planets orbiting Kepler-79 (a.k.a. KOI-152) are smaller than $4 R_\oplus$ and have densities lower than 1.0 g cm^{-3} (Jontof-Hutter et al. 2014). In an intensive *Kepler* follow-up campaign spanning 4 years, Marcy et al. (2014)

* W.M.O. Keck Observatory.

⁹ Ken & Gloria Levy Fellow.

¹⁰ Hubble Fellow.

measured or constrained the masses of 42 small exoplanets using Keck-HIRES, finding many planets that have volatiles and a few planets that might have stony-iron compositions.

The mass measurements listed above allowed the community to probe composition trends within the planet population. Based on the density–radius distribution of 65 exoplanets smaller than Neptune, Weiss & Marcy (2014) found two empirical relations: among planets smaller than $1.5 R_{\oplus}$, density increases nearly linearly with increasing planet radius in a manner consistent with a stony-iron composition like Earth’s. However, bulk density decreases with increasing radius for planets between 1.5 and $4.0 R_{\oplus}$, implying an increasing admixture of volatiles above $1.5 R_{\oplus}$. Rogers (2015) used a hierarchical Bayesian framework to rigorously test the transition from stony-iron planets to planets with a gaseous envelope and found that at and above $1.6 R_{\oplus}$, the majority of planets have a volatile envelope, while the remaining minority are sufficiently dense to be comprised of iron and silicate only. Dressing et al. (2015) measured the mass of Kepler-93 b ($R_p = 1.478 \pm 0.019$, $M_p = 4.02 \pm 0.68$) and determined that Kepler-93 b and the other known rocky planets (Kepler-78 b, Kepler-36 b, Kepler-10 b, and Corot-7 b) all have masses and radii that can be explained with an iron-silicate composition. By contrast, KOI-273 b ($R_p = 1.82 \pm 0.10 R_{\oplus}$, $M_p = 5.46 \pm 2.50 M_{\oplus}$; Gettel et al. 2016) is too big to be rocky and requires a small volatile envelope. Wolfgang & Lopez (2015) used a hierarchical Bayesian model to explore the diversity of planet mass, density, and composition as a function of planet radius. They found that planets smaller than $1.5 R_{\oplus}$ are typically rocky, whereas planets larger than $1.5 R_{\oplus}$ typically require a small fraction of hydrogen gas or other volatiles to explain their densities. Furthermore, small differences in the mass fraction of hydrogen in the planet’s envelope explain the broad range of planet densities at a given radius for planets between 2 and $4 R_{\oplus}$.

Although planets smaller than $1.5 R_{\oplus}$ tend to be stony-iron and planets larger than $1.5 R_{\oplus}$ tend to have at least a small hydrogen envelope, there are exceptions to the pattern. In the Kepler-138 system, which contains three planets smaller than $1.5 R_{\oplus}$, at least one planet, Kepler-138 d ($R_p = 1.212 \pm 0.075 R_{\oplus}$, $M_p = 0.640^{+0.674}_{-0.387} M_{\oplus}$, $\rho_p = 2.1^{+2.2}_{-1.2} \text{ g cm}^{-3}$), has a low enough density to require a volatile envelope (Kipping et al. 2014; Jontof-Hutter et al. 2015). Kepler-138 d is the smallest exoplanet that we know to contain a gaseous envelope.

The Kepler-10 system is a powerful testing ground for our understanding of the compositions of small planets. Kepler-10 is a Sun-like star with slow rotation and little stellar activity (Dumusque et al. 2014). It has two planets discovered via transits in the *Kepler* Mission: Kepler-10 b, which has an orbital period of 0.84 days and radius $1.47 R_{\oplus}$, and Kepler-10 c, which has an orbital period of 45 days and radius $2.35 R_{\oplus}$ (Batalha et al. 2011; Dumusque et al. 2014). Batalha et al. (2011, hereafter B11) measured the mass and bulk density of Kepler-10 b and determined that it was rocky, making this planet the first rocky planet discovered by the *Kepler* Mission, and the second rocky exoplanet discovery. More recently, Dumusque et al. (2014, hereafter D14) reported that Kepler-10 c has a radius of $2.35 R_{\oplus}$, a mass of $17.2 \pm 1.9 M_{\oplus}$, and a density of $7.1 \pm 1.0 \text{ g cm}^{-3}$. Based on its position in the mass–radius diagram, D14 interpreted the composition of Kepler-10 c as mostly rock by mass, with the remaining mass in volatiles of high mean-molecular weight (likely water). They noted,

however, that compositional degeneracy prevented them from determining the precise water fraction.

Kepler-10 c is unusual in that the mass reported in D14 is large compared to other exoplanets its size. Most exoplanets with radii 2.0 – $2.5 R_{\oplus}$ have much lower masses than $17 M_{\oplus}$, with a weighted mean mass of $5.4 M_{\oplus}$ (Weiss & Marcy 2014) in that size range. For example, HD 97658 b, a planet discovered in RVs (Howard et al. 2011a) that was subsequently observed to transit its star, has a radius of $2.34 \pm 0.16 R_{\oplus}$ and a mass of $7.87 \pm 0.73 M_{\oplus}$ (Dragomir et al. 2013). Kepler-68 b has a radius of $2.32 \pm 0.02 R_{\oplus}$ and a mass of $7.15 \pm 2.0 M_{\oplus}$ (Gilliland et al. 2013; Marcy et al. 2014). Although there is a large scatter in the observed masses between 2 and $2.5 R_{\oplus}$, this scatter results from a few low-mass planets of this size. For example, Kepler-11 f, which has a radius of $2.49 \pm 0.06 R_{\oplus}$, has a mass of $2.0^{+0.8}_{-0.9} M_{\oplus}$ (Lissauer et al. 2011, 2013). In contrast, the most massive planet in this size range other than Kepler-10 c is Kepler-131 b. The initial mass measurement of Kepler-131 b (Marcy et al. 2014) was $R_p = 2.41 \pm 0.20 R_{\oplus}$, $M_p = 16.13 \pm 3.50 M_{\oplus}$, resulting in a bulk density of $6.0 \pm 1.98 \text{ g cm}^{-3}$, but additional measurements obtained since publication show the mass to be much smaller; the confusion was from astrophysical rather than instrumental sources (personal communication, H. Isaacson 2016, in preparation). Thus, Kepler-10 c seems to be unusual in its high mass for planets between 2 and $2.5 R_{\oplus}$. All of these planets except Kepler-10 c are included in the empirical mass–radius relation to exoplanets between 1.5 and $4 R_{\oplus}$ ($M_p/M_{\oplus} = 2.69(R_p/R_{\oplus})^{0.93}$; Weiss & Marcy 2014), according to which a planet of size $2.3 R_{\oplus}$ should have a mass of $5.8 M_{\oplus}$.

In this paper, we build on the data and analysis of D14, adhering to the techniques therein as completely as possible but with the addition of 72 RVs from Keck-HIRES, in an effort to calculate a new and improved two-planet orbital solution for the Kepler-10 system. We also notice that Kepler-10 c exhibits TTVs, i.e., perturbations to its orbit, as did Kipping et al. (2015). Because Kepler-10 b is dynamically distant from Kepler-10 c ($P_c/P_b = 54$), Kepler-10 b cannot perturb Kepler-10 c sufficiently to reproduce the observed TTVs. Therefore, we infer the existence of a third planet in the system, planet candidate KOI-72.X, which explains the observed TTVs. We explore various dynamic configurations for KOI-72.X that reproduce the observed TTVs and are consistent with the RVs as well. Finally, we comment on the compositions of Kepler-10 b and Kepler-10 c, and how their masses, radii, and densities compare to those of other small transiting planets.

2. RADIAL VELOCITIES (RVs) OF KEPLER-10 FROM HIRES AND HARPS-N

HIRES has a long history of achieving precision RVs with an rms of $\sim 2 \text{ m s}^{-1}$ on quiet, Sun-like stars over many years of observations (Howard et al. 2010, 2011a, Figure 1). Our group has used HIRES to measure and place upper limits on the masses of many small planets, especially in the *Kepler* era (e.g., Marcy et al. 2014). Because the planets transit and are vetted through a variety of astrophysical techniques, the burden of confirming the planet does not fall entirely to RVs. In this case, Fressin et al. (2011) validated the planetary nature of Kepler-10 c, incorporating the transit shape and depth in multiple passbands, high-resolution imaging and spectroscopy of the host star, and stellar population synthesis to find a conservative

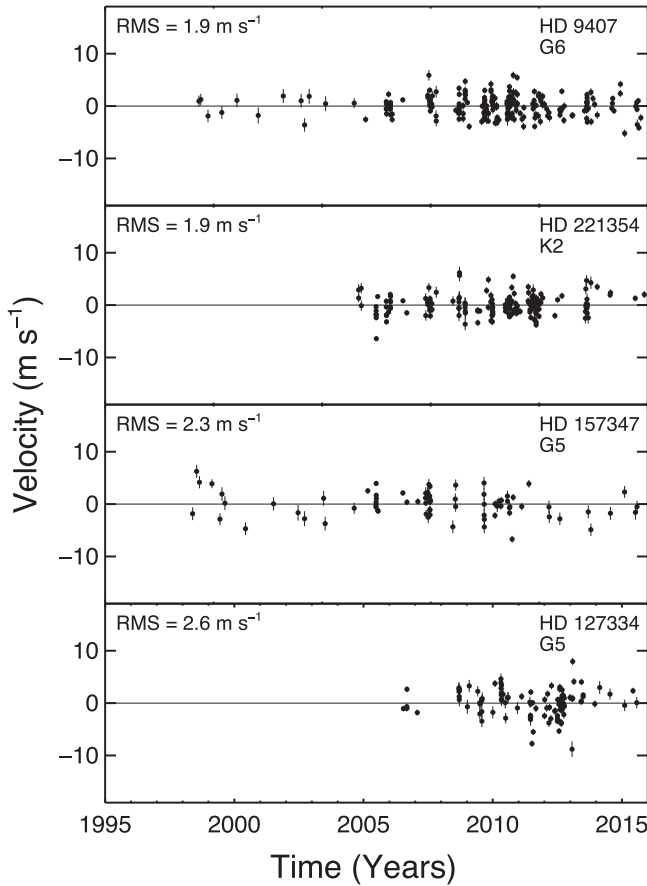


Figure 1. RV vs. time for stable stars observed by Keck-HIRES. The rms of the RVs, stellar name, and stellar spectral type are shown. The typical rms of $\sim 2 \text{ m s}^{-1}$ achieved by Keck-HIRES over a decade for stars without planets demonstrates the ability of HIRES as a multi-season, precision-RV instrument.

false alarm probability of 1.6×10^{-5} . Lissauer et al. (2012) demonstrated the very low probability of having a false alarm planet in a multi-planet system, further reducing the false alarm probability of Kepler-10 c by an order of magnitude. Thus, it is not necessary to determine the mass of Kepler-10 c (or any other statistically validated small planet) with 3σ significance in order to confirm the planet's existence or to make statistically significant claims about the composition of the planet. A mass upper limit might exclude a purely stony-iron composition with 3σ confidence while only being 1σ away from a mass of zero. Such planets provide valuable information about the exoplanet population, and excluding them from population studies on the basis of their large fractional mass uncertainty (σ_m/m) will systematically exclude the low-mass exoplanets. Modern exoplanet mass-radius relations (e.g., Weiss & Marcy 2014; Rogers 2015; Wolfgang & Lopez 2015) incorporate the low-significance mass detections.

Both the HIRES and HARPS-N spectrographs have successfully obtained high-precision RVs of *Kepler* stars in the past (Marcy et al. 2014; Dressing et al. 2015). Notably, two teams used each spectrograph to independently measure the RV signal from the low-mass planet Kepler-78 b. Howard et al. (2013) obtained a mass of $1.69 \pm 0.41 M_{\oplus}$ for Kepler-78 b, and Pepe et al. (2013) obtained a mass of 1.86 ± 0.32 . The independent detections of the RV signal in both spectrometers, and the agreement in the amplitude of that signal, demonstrate

Table 1
RVs of Kepler-10 from HIRES and HARPS-N

BJD (−2454900.0)	RV (m s^{-1})	unc. RV (m s^{-1} , inc. jitter)	S/N	Instrument
173.900499	5.21	4.18	152.8	HIRES
174.877797	0.37	3.94	217.3	HIRES
175.773348	3.31	3.95	214.6	HIRES
176.862854	1.10	3.96	217.1	HIRES
177.923401	−6.28	3.97	222.3	HIRES
178.922398	5.96	3.96	217.8	HIRES
179.972876	0.90	4.00	217.8	HIRES
180.896063	2.56	3.94	216.3	HIRES
181.969271	−9.41	3.96	217.6	HIRES
182.847887	−8.01	3.97	215.8	HIRES
183.760854	−1.30	3.92	217.0	HIRES
183.945387	−3.17	3.99	218.2	HIRES
184.877994	−1.17	3.93	217.0	HIRES
206.889914	0.64	4.04	220.6	HIRES
208.885123	−8.82	4.28	154.1	HIRES
208.890922	−6.76	5.28	80.0	HIRES
211.830107	10.61	4.38	166.7	HIRES
269.71177	−0.59	4.22	152.7	HIRES
269.720925	−0.77	4.08	202.7	HIRES
269.733899	5.59	4.04	215.5	HIRES
270.715114	−0.47	3.99	214.5	HIRES
270.733655	−6.97	3.98	213.4	HIRES
272.756489	3.48	4.03	157.2	HIRES
273.714025	1.35	3.97	198.7	HIRES
273.720425	4.13	5.03	75.4	HIRES
273.727555	−0.49	4.00	193.4	HIRES
412.04715	−3.91	3.94	217.3	HIRES
413.004124	−2.11	3.94	215.9	HIRES
414.004814	−9.03	3.95	215.3	HIRES
415.111272	−0.13	4.12	205.1	HIRES
417.998478	2.79	3.96	215.8	HIRES
418.121283	−2.30	3.93	215.4	HIRES
419.027179	−0.98	4.06	214.7	HIRES
420.062974	2.83	3.95	218.5	HIRES
421.006521	2.53	3.93	218.1	HIRES
421.969467	1.75	3.97	217.7	HIRES
443.050045	−1.13	3.90	241.1	HIRES
444.031958	−1.08	3.93	242.3	HIRES
444.964655	−3.66	4.34	132.4	HIRES
444.977237	−8.96	3.93	241.4	HIRES
445.068315	−3.82	4.00	218.3	HIRES
450.972744	−0.41	3.92	243.6	HIRES
451.987745	−0.93	3.95	242.7	HIRES
473.81361	3.54	3.97	241.1	HIRES
476.86488	−1.89	3.88	313.6	HIRES
479.902118	−0.74	3.98	242.6	HIRES
503.897962	2.84	3.89	313.6	HIRES
505.056086	−4.34	4.06	211.1	HIRES
507.012774	−1.30	3.92	311.8	HIRES
511.985723	−4.08	3.86	314.8	HIRES
512.805268	−4.57	3.86	314.4	HIRES
514.80255	−4.50	3.93	281.8	HIRES
1172.682384	−2.70	3.05	56.2	HARPS-N 1
1172.704768	−3.04	3.11	53.4	HARPS-N 1
1187.57572	−1.67	3.32	45.0	HARPS-N 1
1187.596901	4.37	3.18	48.5	HARPS-N 1
1203.106739	−5.79	3.90	312.2	HIRES
1203.661644	−0.55	3.45	38.7	HARPS-N 1
1203.689793	−4.47	3.32	41.9	HARPS-N 1
1215.691945	−3.45	3.04	60.6	HARPS-N 1
1215.713149	−7.55	3.22	52.5	HARPS-N 1
1216.704755	2.06	4.47	28.4	HARPS-N 1
1216.719003	−2.56	4.77	26.5	HARPS-N 1

Table 1
(Continued)

BJD (−2454900.0)	RV (m s ^{−1})	unc. RV (m s ^{−1} , inc. jitter)	S/N	Instrument
1225.568254	−7.06	3.76	35.2	HARPS-N 1
1225.589446	−8.06	3.31	44.2	HARPS-N 1
1226.447899	−2.83	2.94	59.4	HARPS-N 1
1226.664948	−0.54	4.53	28.7	HARPS-N 1
1227.422428	−13.21	9.66	13.9	HARPS-N 1
1227.441641	0.41	2.91	62.7	HARPS-N 1
1228.43499	2.16	2.95	60.1	HARPS-N 1
1228.560476	−2.77	2.94	59.7	HARPS-N 1
1228.662918	−1.70	3.14	49.7	HARPS-N 1
1248.408122	7.45	3.22	43.5	HARPS-N 1
1248.511779	10.45	3.06	48.5	HARPS-N 1
1248.617819	3.48	3.05	53.9	HARPS-N 1
1251.396386	−0.48	3.33	42.5	HARPS-N 1
1252.407893	1.01	2.84	67.9	HARPS-N 1
1252.640275	0.59	3.36	45.4	HARPS-N 1
1253.395106	2.11	2.98	54.3	HARPS-N 1
1253.493404	−5.91	4.83	25.1	HARPS-N 1
1253.647013	4.45	2.97	58.8	HARPS-N 1
1260.473487	−1.01	4.25	31.4	HARPS-N 1
1260.626355	−3.28	3.98	34.8	HARPS-N 1
1261.39719	−4.78	3.42	40.7	HARPS-N 1
1261.573183	−5.06	3.65	38.9	HARPS-N 1
1262.394398	−8.23	3.33	43.4	HARPS-N 1
1262.487962	−6.97	3.28	45.2	HARPS-N 1
1262.567972	−9.35	3.47	42.1	HARPS-N 1
1264.385261	1.87	3.27	44.4	HARPS-N 1
1265.380836	3.11	3.27	45.0	HARPS-N 1
1266.384814	3.74	3.45	38.9	HARPS-N 1
1266.534418	−4.07	3.36	42.0	HARPS-N 1
1266.601002	−4.84	3.48	40.9	HARPS-N 1
1272.8013	0.67	3.91	283.2	HIRES
1275.410615	4.18	2.84	67.5	HARPS-N 1
1275.521886	3.13	2.97	58.3	HARPS-N 1
1278.373888	−5.11	3.09	49.5	HARPS-N 1
1278.494638	5.83	3.03	53.7	HARPS-N 1
1279.373462	3.53	2.91	58.8	HARPS-N 1
1279.521052	4.21	3.02	57.6	HARPS-N 1
1280.40035	5.13	2.84	70.7	HARPS-N 1
1280.543831	2.94	2.97	60.5	HARPS-N 1
1281.435709	−0.84	2.81	73.4	HARPS-N 1
1281.529573	−16.52	9.34	16.1	HARPS-N 1
1281.534515	3.71	2.98	61.3	HARPS-N 1
1282.398292	1.78	2.86	64.9	HARPS-N 1
1282.535095	−1.19	2.98	58.3	HARPS-N 1
1283.373536	0.00	3.23	44.7	HARPS-N 1
1283.560153	4.16	3.08	53.2	HARPS-N 1
1345.332519	−8.77	2.93	60.6	HARPS-N 2
1352.34146	−0.79	2.98	66.6	HARPS-N 2
1479.677427	0.46	3.32	53.2	HARPS-N 2
1479.750484	−0.28	3.25	54.8	HARPS-N 2
1480.663449	−3.22	3.18	55.6	HARPS-N 2
1480.739863	−4.57	3.06	61.1	HARPS-N 2
1481.685619	−6.27	2.94	72.1	HARPS-N 2
1481.75076	−7.68	2.94	72.0	HARPS-N 2
1482.671897	−7.20	2.88	75.3	HARPS-N 2
1482.753519	−6.84	3.00	66.5	HARPS-N 2
1496.608742	4.82	2.86	80.9	HARPS-N 2
1496.724487	4.77	2.84	83.1	HARPS-N 2
1498.614845	6.52	3.41	51.1	HARPS-N 2
1498.727696	2.65	3.09	60.7	HARPS-N 2
1500.594327	−8.64	11.61	14.9	HARPS-N 2
1502.590476	10.89	5.82	26.6	HARPS-N 2
1502.707713	3.53	7.95	20.0	HARPS-N 2

Table 1
(Continued)

BJD (−2454900.0)	RV (m s ^{−1})	unc. RV (m s ^{−1} , inc. jitter)	S/N	Instrument
1518.588709	−1.60	3.27	49.9	HARPS-N 2
1518.689186	−0.56	3.19	50.1	HARPS-N 2
1520.585042	2.13	3.89	37.1	HARPS-N 2
1520.698459	−3.86	3.03	59.1	HARPS-N 2
1521.589725	−1.62	2.92	68.8	HARPS-N 2
1521.686301	−0.71	2.75	90.7	HARPS-N 2
1532.559497	−2.57	2.81	78.4	HARPS-N 2
1532.704814	−6.82	2.78	84.1	HARPS-N 2
1533.562499	−6.26	2.79	83.9	HARPS-N 2
1533.708811	−9.88	2.76	88.1	HARPS-N 2
1534.523174	−10.66	3.12	57.1	HARPS-N 2
1534.689787	−5.63	2.85	73.0	HARPS-N 2
1536.539212	−4.64	2.83	78.5	HARPS-N 2
1536.69836	−1.89	2.80	81.7	HARPS-N 2
1537.537063	−5.45	2.85	75.3	HARPS-N 2
1537.698873	−4.10	2.78	84.5	HARPS-N 2
1562.440914	0.95	3.05	60.9	HARPS-N 2
1562.595327	2.52	3.04	60.7	HARPS-N 2
1563.499671	4.82	3.07	58.3	HARPS-N 2
1563.673401	−1.63	2.94	63.5	HARPS-N 2
1564.515083	5.04	4.85	29.9	HARPS-N 2
1564.675676	−0.53	3.33	49.0	HARPS-N 2
1565.523526	−1.72	3.13	56.4	HARPS-N 2
1566.47765	−1.59	2.94	67.5	HARPS-N 2
1566.698684	0.74	2.96	67.4	HARPS-N 2
1578.422373	−1.78	3.08	59.9	HARPS-N 2
1578.607224	1.29	2.91	71.5	HARPS-N 2
1579.468298	1.48	2.81	83.0	HARPS-N 2
1579.606263	−1.48	2.81	84.3	HARPS-N 2
1580.550925	−2.58	2.78	86.3	HARPS-N 2
1580.702582	−4.15	2.85	79.9	HARPS-N 2
1581.443399	−4.66	2.94	67.5	HARPS-N 2
1581.578226	−4.45	3.23	53.2	HARPS-N 2
1582.444149	−1.68	3.15	56.2	HARPS-N 2
1582.62878	0.83	3.67	42.6	HARPS-N 2
1595.439337	3.83	2.82	82.7	HARPS-N 2
1595.606467	1.79	2.95	68.4	HARPS-N 2
1596.385682	5.56	2.92	71.5	HARPS-N 2
1596.639015	4.24	2.87	77.4	HARPS-N 2
1597.498195	−0.38	2.80	85.5	HARPS-N 2
1597.67948	2.83	2.89	75.6	HARPS-N 2
1598.494932	7.64	2.84	81.0	HARPS-N 2
1598.671622	4.95	3.06	62.1	HARPS-N 2
1599.444782	6.99	2.88	75.5	HARPS-N 2
1599.669099	7.67	2.97	69.9	HARPS-N 2
1600.450037	5.89	2.85	79.3	HARPS-N 2
1600.634886	1.53	3.08	62.8	HARPS-N 2
1601.425511	−2.03	3.08	61.1	HARPS-N 2
1601.65852	1.59	3.08	62.6	HARPS-N 2
1610.395668	4.14	3.36	48.7	HARPS-N 2
1610.406339	6.97	3.29	50.2	HARPS-N 2
1611.547768	−0.14	2.97	66.5	HARPS-N 2
1612.49135	0.09	2.84	79.8	HARPS-N 2
1613.483021	0.44	2.83	80.6	HARPS-N 2
1628.459887	−0.04	3.08	60.1	HARPS-N 2
1628.564955	0.51	3.16	58.7	HARPS-N 2
1629.480763	0.57	2.83	83.6	HARPS-N 2
1629.614778	3.18	3.24	57.0	HARPS-N 2
1630.444186	2.22	2.82	84.2	HARPS-N 2
1630.53025	2.92	2.87	77.3	HARPS-N 2
1654.373345	3.44	3.01	56.8	HARPS-N 2
1654.46788	−0.74	2.98	58.8	HARPS-N 2
1657.371082	−0.12	2.77	84.4	HARPS-N 2

Table 1
(Continued)

BJD (−2454900.0)	RV (m s ^{−1})	unc. RV (m s ^{−1} , inc. jitter)	S/N	Instrument
1657.503069	−0.78	3.10	58.0	HARPS-N 2
1662.435891	−2.10	3.61	45.0	HARPS-N 2
1663.373238	−2.36	2.89	71.8	HARPS-N 2
1663.472796	−4.30	3.04	62.5	HARPS-N 2
1665.352941	−4.94	2.97	66.8	HARPS-N 2
1665.482578	1.24	2.82	81.1	HARPS-N 2
1667.347572	3.21	2.77	88.3	HARPS-N 2
1671.344738	−1.73	3.37	48.5	HARPS-N 2
1671.455024	−0.97	3.35	49.9	HARPS-N 2
1680.342329	−0.12	2.89	70.8	HARPS-N 2
1680.43589	−3.70	2.93	69.6	HARPS-N 2
1682.32927	−2.72	2.80	81.4	HARPS-N 2
1682.376757	0.14	2.96	66.8	HARPS-N 2
1926.898038	4.23	3.89	283.4	HIRES
1942.001946	2.24	3.95	283.1	HIRES
1942.954468	4.33	3.92	283.4	HIRES
1943.951042	−2.30	3.89	284.7	HIRES
1962.874534	−0.57	3.89	286.0	HIRES
1963.860172	0.82	3.90	283.8	HIRES
1964.900473	0.11	3.93	283.4	HIRES
1965.945739	−2.07	3.90	282.6	HIRES
1982.934778	0.23	3.86	281.7	HIRES
1983.770615	6.05	3.93	280.2	HIRES
1989.012469	1.35	3.90	282.4	HIRES
2006.909888	4.64	3.88	280.8	HIRES
2007.77185	4.84	3.81	283.8	HIRES
2008.976767	14.31	4.49	131.4	HIRES
2009.88478	10.16	3.85	280.9	HIRES
2013.741571	6.44	3.84	285.1	HIRES
2251.114854	1.77	3.90	280.9	HIRES
2280.075021	−0.34	3.93	277.9	HIRES

Note. Jitter has already been applied to the RV uncertainties. Offsets between the RV data sets have been applied. HARPS-N 1 refers to the pre-upgrade CCD (before 2012 September 21). HARPS-N 2 refers to the post-upgrade CCD (after 2012 November 12).

that both the HIRES and HARPS-N spectrometers are capable of accurately and precisely measuring low-amplitude RV signals.

Ground-based RV follow-up of Kepler-10 has been ongoing since Kepler-10 b and Kepler-10 c were discovered. B11 presented 52 RVs obtained on Keck-HIRES in 2009–2010, the first seasons after Kepler-10 b and c were discovered, and D14 presented 148 RVs obtained on TNG-HARPS-N that span the summers of 2012–2013. The early measurements presented in B11 targeted the quadrature times of planet b, whereas the later measurements from D14 targeted the quadrature times of planet c.

We present 20 additional RVs from 2014–2015 which, in combination with all the previous RVs, comprise the largest dataset of Kepler-10 RVs to date of 220 RVs total (Table 1 and Figure 2). HARPS-N, which is a fiber-fed, thermally stable spectrometer in a vacuum, achieves better velocity precision at given signal-to-noise than the HIRES spectrometer, but the larger aperture of the Keck telescope (10 m compared to 3.6 m) collects more photons. Thus, both telescope-spectrometer setups achieve a velocity precision of a few m s^{−1} per half hour observing Kepler-10.

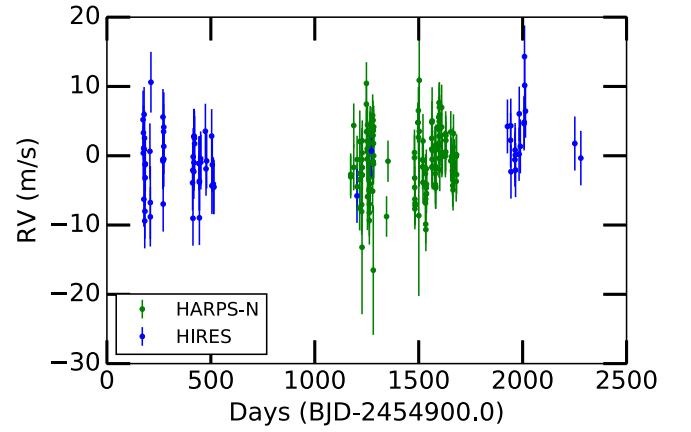


Figure 2. Radial velocity measurements of Kepler-10 from the HIRES (blue) and HARPS-N (green) high-resolution echelle spectrometers.

Although only 20 RVs were taken since the publication of D14, combining all the data provides several major advantages over either the B11 or D14 data alone. Because the *Kepler* field is best accessible during the summer, the data from both HIRES and HARPS-N are clumped in intervals of 2–3 months, a timescale barely longer than the orbital period of Kepler-10 c (45.3 days). Observing just 1–2 orbits of planet c could be problematic if the stellar rotation period is comparable to the orbital period of planet c and temporarily phases with the orbit of planet c over a few rotation cycles. Furthermore, incomplete observing phase coverage combined with noise can result in additional power in an alias of the planetary signal or a peak resulting from the window function (Dawson & Fabrycky 2010; Rajpaul et al. 2015). The combined data cover observing phase as a function of sidereal day, solar day, and solar year better than either data set does alone (see Figure 3), improving our resilience to noise manifesting in monthly and yearly aliases of planet c’s orbit. Furthermore, the combined baseline of 6 years (2009–2015) is much longer than the 2-year baseline achieved in either of the previous papers. The long observing baseline helps to average out possible spurious signals that can arise from stellar activity on the timescales of stellar rotation and convection (~ 1 month). The long baseline also improves our sensitivity to possible long-period signals. These advantages motivate combining all of the reliable data.

2.1. HIRES Doppler Pipeline

We calculate precise RVs of Kepler-10 using the standard Doppler code of the CPS group (Howard et al. 2011b) with the inclusion of a new de-trending routine. Previously published RVs (B11) were collected during the 2009–2010 observing seasons. Subsequent observations were taken in the 2014 observing season. Long term RV precision spanning 10 years is consistently achieved with HIRES as described in Howard et al. (2011b). Exposure times of ~ 30 minutes are required to achieve S/N ~ 200 in the iodine region, resulting in internal RV errors of 1.5–2.0 m s^{−1}. Each observation uses a slit with dimensions of $0''.87 \times 14''.0$ yielding a resolving power of 60,000, and allowing for subtraction of night sky emission lines, and scattered moonlight.

During the initial RV extraction we model the instrumental point-spread function (PSF) as a sum of 13 Gaussians with positions and widths fixed but their heights free to vary (Butler et al. 1996). Any correlations in the final RVs with the heights

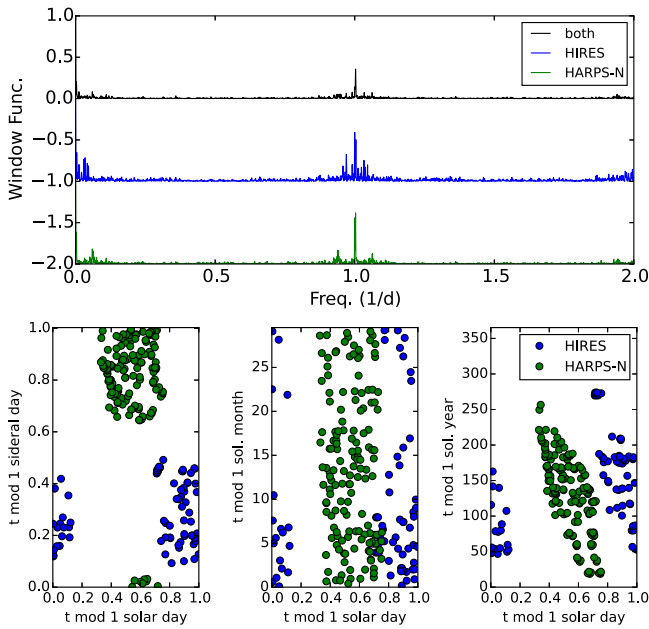


Figure 3. Top: window function of the combined RVs, HIRES RVs, and HARPS-N RVs, vertically offset for clarity. The peaks near 1/day indicate the daily alias in each data set, and the peaks near 0.06/day are consistent with a monthly alias. The combined RVs reduce the strength of the daily alias and remove the monthly alias. Bottom left: time of observation modulo the sidereal day vs. time of observation modulo the solar day shows the sidereal and solar daily phase coverage of the observations from HIRES (blue) and HARPS-N (green). Bottom center: same as bottom left, but with time modulo the solar month on the dependent axis. Bottom right: same as bottom left, but with time modulo the solar year on the dependent axis.

of these Gaussians (PSF parameters) likely indicate small inadequacies of our PSF model to completely describe the shape of the instrumental PSF. RV shifts caused by the gravitational influence of orbiting bodies should not be correlated with the shape of the instrumental PSF.

In order to clean the RVs of any possible systematic trends we detrend the final RVs by removing correlations with the instrumental PSF parameters, the magnitude of the RV uncertainty, and the signal-to-noise ratio (S/N) of the spectrum. After masking any 5σ outliers, we search for significant correlations by calculating the Spearman rank correlation coefficient for each of these variables with RV (Spearman1904). We take note of any parameters that show a correlation coefficient greater than 0.1 and include these variables in a multivariate ordinary least squares linear regression using the STATSMODELS¹¹ package in Python. This final multidimensional surface is then subtracted from the final RVs. This technique improves the rms of the RV time series of Kepler-10 from 4.9 to 4.6 m s^{-1} by detrending against nine PSF parameters and the S/N ratio of the spectra. To check that the detrending algorithm does not accidentally remove the signal of the planets, we calculated a two-planet circular fit to both the detrended and non-detrended RVs. The rms of the change in RV introduced by the detrending algorithm was 1.2 m s^{-1} (i.e., less than the uncertainty in each RV), and the solutions for all parameters were consistent within 0.1 m s^{-1} (much less than our 1σ uncertainties in the parameters). We do not add the random noise introduced by the detrending algorithm to our error budget because our technique for

solving for the jitter (see Equation (1)) naturally incorporates the uncertainties that arise through this method.

2.2. Analysis of the HIRES and HARPS-N RVs

Figure 4 shows the Kepler-10 RVs from HIRES and HARPS-N phase-folded to the orbital periods of the two transiting planets, with red diamonds indicating the weighted mean RV in bins of 0.1 orbital phases to guide the eye. Figure 5 shows the MCMC posterior distributions of two-planet circular fits to the HIRES RVs alone (blue) and the HARPS-N RVs alone (green). A summary of the best fit parameters to the HIRES RVs alone are given in Table 2. The HIRES RVs yield $m_c = 5.69^{+3.19}_{-2.90} M_{\oplus}$, a result that disagrees with the best fit to the HARPS-N RVs ($m_c = 17.2 \pm 1.9$) by 3.1σ .

2.3. Analysis of the Discrepancy between HIRES and HARPS-N RVs

What is the source of the discrepancies between K_b and K_c in the HIRES and HARPS-N data? HIRES RVs are stable with an rms of 2 m s^{-1} for various stars of spectral types without any known planets over decades (Figure 1). Removing 2.5σ outliers changes K_b and K_c by 1%, an insignificant amount compared to our uncertainties. We do not find any significant correlations between the RVs and barycentric correction, or between the RVs and stellar activity indices, in either the HIRES or HARPS-N data.

When we break either the HIRES or HARPS-N data into two epochs (first half versus second half of the acquired RVs), both spectrometers find significantly different values of K_b and/or K_c in the first versus the second half of their RV data. Using just the first half of the HIRES data, we find $K_{b,1} = 4.07 \pm 0.95 \text{ m s}^{-1}$, $K_{c,1} < 1.10 \text{ m s}^{-1}$ (68% confidence). Using just the second half of the HIRES RVs, we get $K_{b,2} = 2.67 \pm 0.88 \text{ m s}^{-1}$, $K_{c,2} = 1.48 \pm 0.80 \text{ m s}^{-1}$. For HARPS-N, we divided the RVs into those taken before and after 2012 November 12 (the date of their CCD upgrade, which is a convenient division time). Using just the pre-upgrade HARPS-N data, we find $K_{b,1} = 3.29 \pm 0.62 \text{ m s}^{-1}$, $K_{c,1} = 2.25 \pm 0.59 \text{ m s}^{-1}$. Using just the post-upgrade HARPS-N RVs, we get $K_{b,2} = 2.02 \pm 0.37 \text{ m s}^{-1}$, $K_{c,2} = 3.71 \pm 0.41 \text{ m s}^{-1}$ (see Figure 6). The 1.7σ difference in K_b and 2.0σ difference K_c between the pre- and post-upgrade RVs from HARPS-N is larger than we would expect from statistical fluctuations alone. The apparent change in K_b and K_c suggests that an additional, time-correlated source, possibly from stellar activity or the presence of additional planets, confounds both the HIRES and HARPS-N spectrometers on short timescales.

3. PLANETARY PROPERTIES OF KEPLER-10: TWO-PLANET SOLUTIONS

The significant discrepancy between the best two-planet fits to the HIRES and HARPS-N data sets motivates a reanalysis of the data. Since we cannot find evidence that either data set is compromised, we choose to combine all the available data from HIRES and HARPS-N to calculate the most up-to-date planet masses. For consistency and relevant comparison to previous findings, we adopt the Kepler-10 stellar properties from D14, which are listed in Table 7.

¹¹ <https://pypi.python.org/pypi/statsmodels>

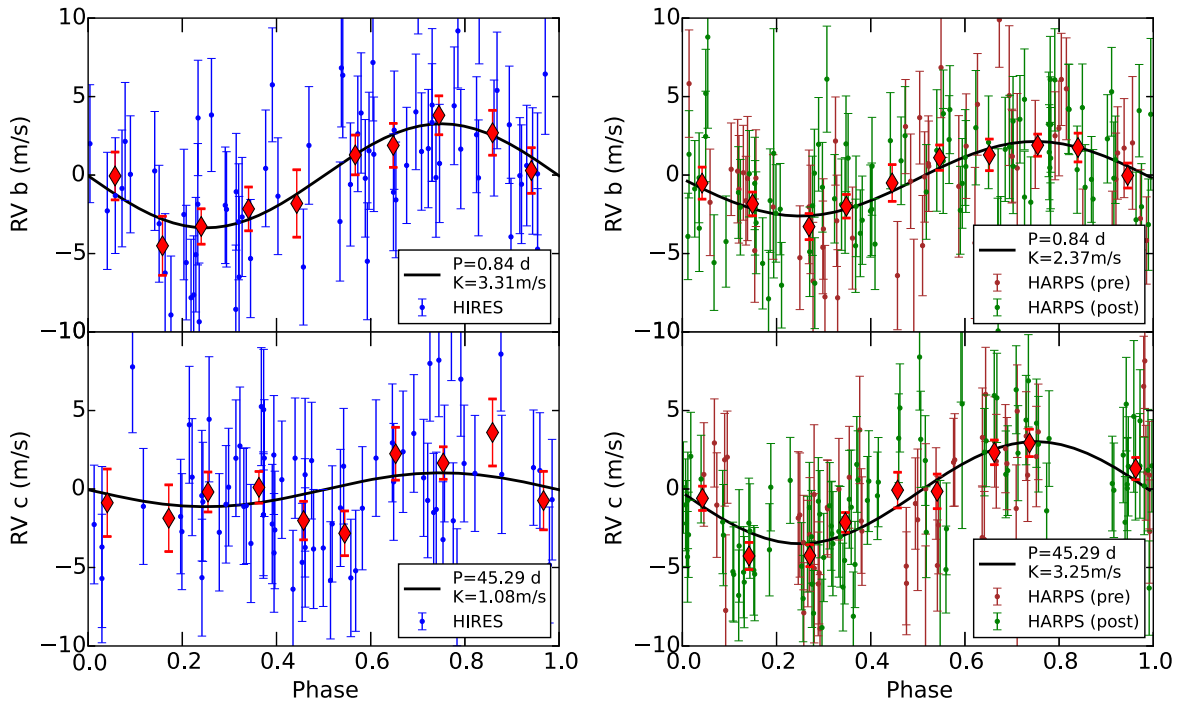


Figure 4. Left: the RVs from HIRES phase-folded to the orbital periods of Kepler-10 b (top) and c (bottom). The red diamonds show the weighted mean RV of the HIRES data in bins of 0.1 orbital phase. The black curve shows the best two-planet circular fit: $K_b = 3.31 \text{ m s}^{-1}$, $K_c = 1.08 \text{ m s}^{-1}$. Right: same as left, but using the pre-CCD upgrade (brown) and post-CCD upgrade (green) HARPS-N RVs. Our best two-planet circular fit yields $K_b = 2.37 \text{ m s}^{-1}$, $K_c = 3.25 \text{ m s}^{-1}$, in agreement with Dumusque et al. (2014).

3.1. Two-planet Circular Fit

The RV signals produced by small planets are often too low-amplitude, compared to the typical RV noise, to precisely measure their orbital eccentricities. Thus, the RVs of many of the systems of small planets discovered by *Kepler* and RV surveys (e.g., Eta-Earth) are consistent with planets in circular or nearly circular orbits. We are motivated to explore a two-planet circular orbit because the RVs do not demand eccentric orbits for either Kepler-10 b or Kepler-10 c. Furthermore, B11 and D14 model the Kepler-10 system with circular orbits, so we explore a two-planet circular fit to enable a direct comparison to their results.

The photometrically determined transit times from *Kepler* constrain the orbital ephemerides of Kepler-10 b and c. Specifically, the photometry precisely constrains the time of transit, orbital period, and inclination of each planet. The remaining free dynamical parameter for each planet is the mass. We solve for the mass via the observable semi-amplitude of the RV sinusoid, K .

In addition to the dynamical parameters, fitting RVs from two different spectrographs incurs several nuisance parameters. There is a zero point offset for each set of RVs. Each measured RV has some internal uncertainty, plus error of astrophysical origin (from stellar oscillations, plage, starspots, magnetic activity, etc.), plus additional errors from the spectrometer. For each spectrometer, we report the combined astrophysically-induced error and spectrometer-induced error as a jitter term, σ_{jitter} , which we add in quadrature with the internal uncertainty in the RV to obtain the total uncertainty of each RV. The internal uncertainty of the RV varies from measurement to measurement, whereas the jitter term is the same for all RVs taken by a single spectrometer.

Therefore, the two-planet circular fit has seven free parameters: the semi-amplitude of the RVs resulting from planet b (K_b), the semi-amplitude of the RVs resulting from planet c (K_c), the velocity zero-point of the RVs (γ), an offset between the RVs taken by the HIRES spectrograph and the RVs taken on the pre-upgrade HARPS-N CCD (offset 1), an offset between the RVs taken by the HIRES spectrograph and the RVs taken on the post-upgrade HARPS-N CCD (offset 2), the jitter of the HIRES spectrograph (j_1) and the jitter of the HARPS-N spectrograph (j_2). The orbital period, time of transit, and orbital inclination were derived from photometry in D14, and we fix them at the values published therein.

To determine the best circular fit to the data, we adopt the same likelihood function as D14:

$$\mathcal{L} = \prod_i \frac{1}{\sqrt{2\pi(\sigma_i^2 + \sigma_j^2)}} \exp\left[-\frac{(\text{RV}_i - \text{RV}_{\text{mod},i})^2}{2(\sigma_i^2 + \sigma_j^2)}\right] \quad (1)$$

where RV_i is the i th observed RV, $\text{RV}_{\text{mod},i}$ is the i th modeled RV, σ_i is the uncertainty in the i th observed RV, and σ_j is the jitter term from the instrument on which the observation was made (either HIRES or HARPS). We minimized the negative log-likelihood via the Levenberg–Marquardt method with the Python package lmfit.

We performed a Markov Chain Monte Carlo (MCMC) analysis to understand the full posterior distribution of the dynamical parameters and their covariances. We used the Python package emcee (Foreman-Mackey et al. 2013), an affine-invariant MCMC sampler. We adopted uniform priors in j_1 , j_2 , γ , offset 1, offset 2, K_b , and K_c , while restricting j_1 , j_2 , K_b , $K_c > 0$. Our dynamical equations, choice of parameters, and the priors on those parameters were chosen to

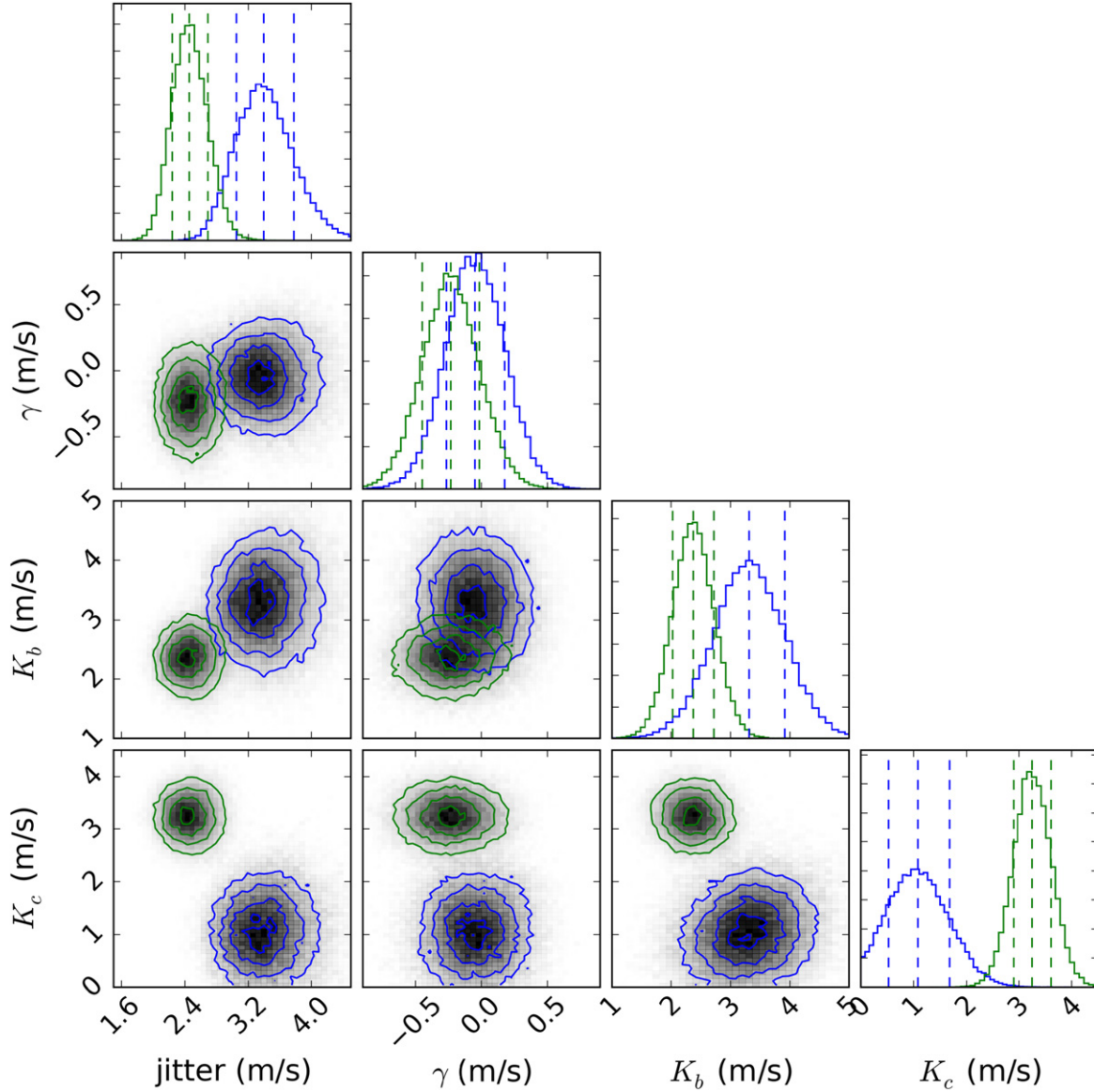


Figure 5. MCMC posterior distributions of two-planet circular fits to the HIRES RVs alone (blue) and the HARPS-N RVs alone (green). The parameters are jitter, the RV zero-point offset γ , and the RV semi-amplitudes from planets b (K_b) and c (K_c). Dashed lines denote the 16th, 50th, and 84th percentiles.

Table 2
Two-planet Circular Fit to Only HIRES RVs

Parameter	Units	Median	+1 σ	-1 σ	References
jitter	m s ⁻¹	3.41	0.39	0.34	A
γ	m s ⁻¹	-0.05	0.22	0.22	A
K_b	m s ⁻¹	3.31	0.59	0.59	A
K_c	m s ⁻¹	1.09	0.61	0.55	A
m_b	M_\oplus	4.61	0.83	0.83	A, B
m_c	M_\oplus	5.69	3.19	2.9	A, B
r_b	R_\oplus	1.47	0.03	0.02	B
r_c	R_\oplus	2.35	0.09	0.04	B
ρ_b	g cm ⁻³	8.0	1.43	1.44	A, B
ρ_c	g cm ⁻³	2.42	1.36	1.24	A, B

Note. All parameters were explored with uniform priors.

References. (A) This work. (B) Dumusque et al. (2014).

replicate D14 as closely as possible, while allowing the inclusion of the HIRES RVs.

The posterior of the MCMC sampler is shown in Figure 7. The two-planet circular fit using the parameters from the median of the posterior distribution is shown in Figure 8. The best two-planet circular fit yields $m_b = 3.72 \pm 0.42 M_\oplus$, $m_c = 13.98 \pm 1.79 M_\oplus$, $\rho_b = 6.46 \pm 0.73 \text{ g cm}^{-3}$, and $\rho_c = 5.94 \pm 0.76 \text{ g cm}^{-3}$. Table 3 lists the median and 1σ uncertainties of the marginalized parameters and derived planet masses and densities.

We computed the Lomb–Scargle (L–S) periodogram of the combined HIRES and HARPS-N RVs using the fasper algorithm (Press & Rybicki 1989, see Figure 9). The most prominent peak was at 0.84 days, the orbital period of planet b. We subtracted the RV component from Kepler-10 b (as determined by our maximum-likelihood model) and computed

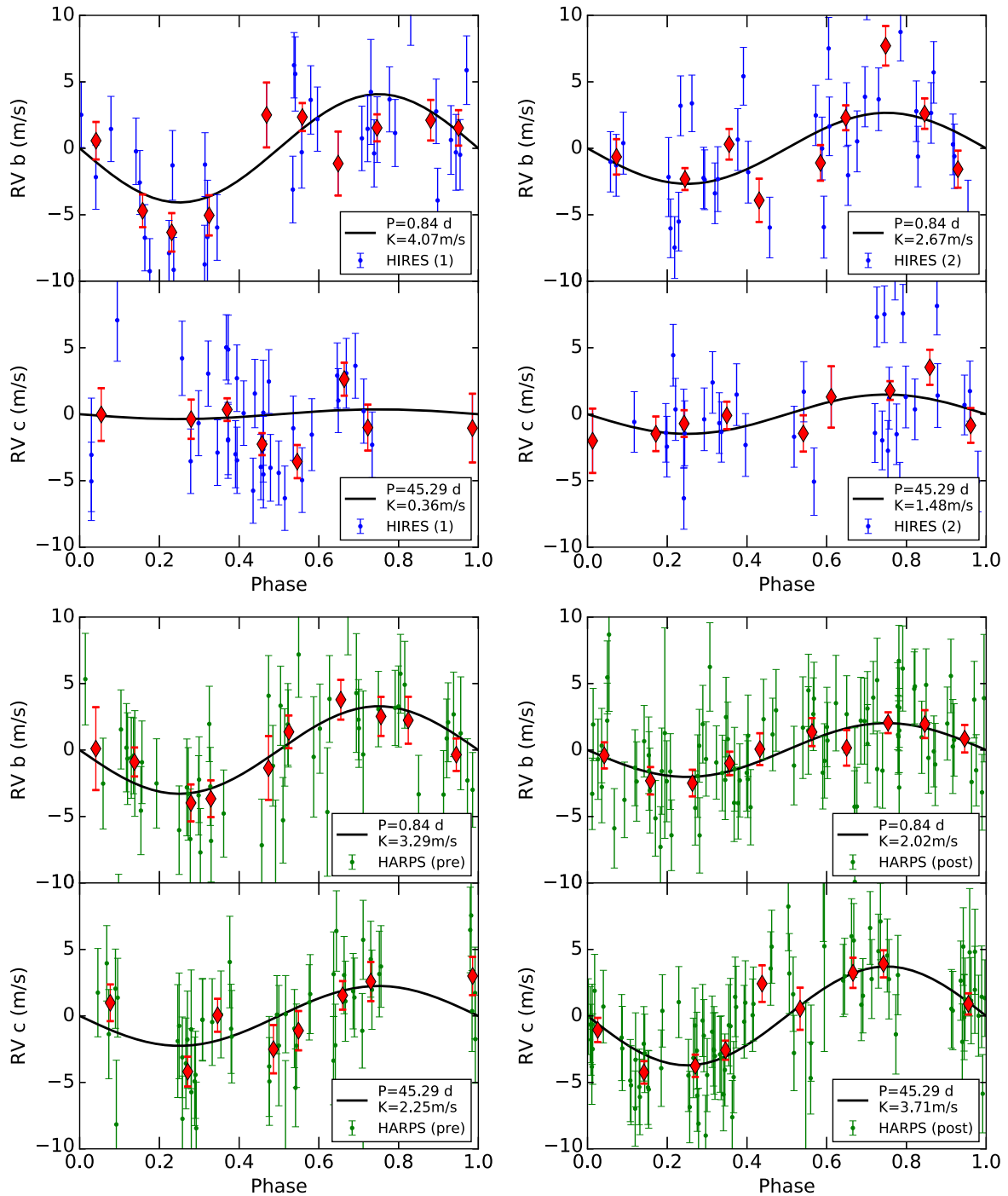


Figure 6. The RV curve of Kepler-10 phase-folded to the orbital periods of planets b and c, for four different subsets of the data: the first half of the HIRES data (top left, $K_b = 4.07 \pm 0.95 \text{ m s}^{-1}$, $K_c = 0.36 \pm 0.7 \text{ m s}^{-1}$), the second half of the HIRES data (top right, $K_b = 2.67 \pm 0.88 \text{ m s}^{-1}$, $K_c = 1.48 \pm 0.80 \text{ m s}^{-1}$), the HARPS-N data from before their CCD upgrade (bottom left, $K_b = 3.29 \pm 0.62 \text{ m s}^{-1}$, $K_c = 2.25 \pm 0.59 \text{ m s}^{-1}$), and the HARPS-N data from after their CCD upgrade (bottom right, $K_b = 2.02 \pm 0.37 \text{ m s}^{-1}$, $K_c = 3.71 \pm 0.41 \text{ m s}^{-1}$). The derived values of the RV semi-amplitude, K , for both planets b and c are different by more than 1 m s^{-1} ($\sim 30\%$) from the two halves of the RV data sets from each spectrometer. These inconsistencies within each spectrometer indicate some time-correlated contribution to the RVs, perhaps from stellar activity, additional planets, or systematic RV errors at the level of $\sim 1 \text{ m s}^{-1}$ in the spectrometers.

the periodogram of the residuals, finding a pair of peaks at 44.8 and 51.5 days. The orbital period of planet c is 45.3 days; the peak at 51.5 day is a one-year alias of the orbital period of planet c, intensified by noise in the manner described in Dawson & Fabrycky (2010). We subtracted the model RVs of planet c and computed the periodogram of the residuals, finding a forest of peaks from 13 to 100 days.

3.2. Two-planet Fit with Eccentricity for Planet c

Kepler-10 b, which has an ultra-short orbital period of 0.84 days, very likely has a circular orbit because its circularization timescale is much shorter than the stellar age (B11). However, Kepler-10 c has a sufficiently long orbital period (45.3 days) to maintain a moderately eccentric orbit over the system age. Because we cannot rule out a moderately eccentric orbit for

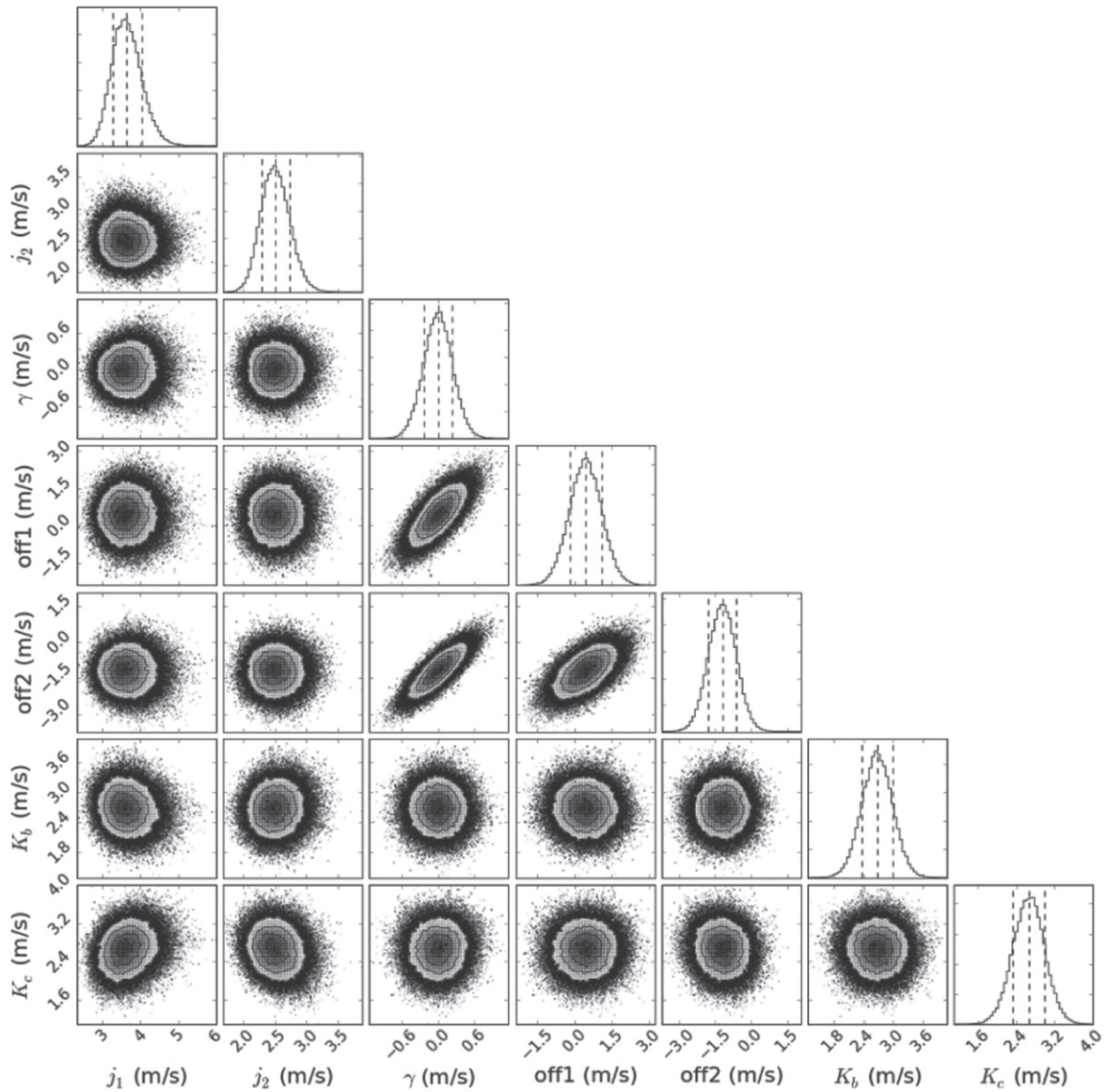


Figure 7. Posterior distribution for the two-planet circular fit to Kepler-10 RVs. Variables are the jitter of the HIRES instrument (j_1), jitter of the HARPS-N instrument (j_2), velocity zero point (γ), velocity offset between HIRES and the HARPS-N RVs from before the CCD upgrade (off1), velocity offset between HIRES and the HARPS-N RVs from after the CCD upgrade (off2), and the semi-amplitudes of the RV curve for planets b (K_b) and c (K_c). The dashed lines indicate the 16th, 50th, and 84th percentiles.

Kepler-10 c, we explore possible two-planet fits in which the orbit of planet c (but not planet b) is allowed to be eccentric.

The two-planet fit in which planet c is allowed eccentricity has two free parameters in addition to the free parameters of the circular fit: $\sqrt{e_c} \cos \omega_c$ and $\sqrt{e_c} \sin \omega_c$. These parameters are a combination of the Keplerian orbital parameters e_c (the eccentricity of planet c) and ω_c (the argument of periastron passage of planet c). We adopted a uniform prior on $\sqrt{e_c} \cos \omega_c$ and $\sqrt{e_c} \sin \omega_c$ with the constraint $(\sqrt{e_c} \cos \omega_c)^2 + (\sqrt{e_c} \sin \omega_c)^2 \leq 1$. The time of periastron passage is determined by a combination of the argument of periastron passage (ω_c), the eccentricity (e_c), the time of transit ($T_{t,c}$), and the orbital period (P).

For the parameters j_1 , j_2 , γ , offset, K_b , and K_c , we adopt uniform priors with the same boundaries as listed for the two-planet circular fit.

We perform an MCMC analysis over j_1 , j_2 , γ , offset 1, offset 2, K_b , K_c , $\sqrt{e_c} \cos \omega_c$, and $\sqrt{e_c} \sin \omega_c$. The posterior

distribution of our sampler is shown in Figure 10. The two-planet fit using the parameters from the maximum likelihood of the posterior distribution is shown in Figure 11. The best two-planet fit allowing eccentricity for planet c yields $m_b = 3.76 \pm 0.43 M_\oplus$, $m_c = 14.59 \pm 1.90 M_\oplus$, $\rho_b = 6.53 \pm 0.75 \text{ g cm}^{-3}$, $\rho_c = 6.21 \pm 0.81 \text{ g cm}^{-3}$, and $e_c = 0.17 \pm 0.13$. Table 4 lists the median and 1σ uncertainties of the marginalized parameters and derived orbital and physical quantities.

4. TRANSIT TIMES OF KEPLER-10 c

The transit times of Kepler-10 c vary with respect to a linear ephemeris. Kipping et al. (2015) found TTVs in the long and short cadence data with 5σ confidence. We independently measure the TTVs and find a solution consistent with the TTVs in Kipping et al. (2015, see Figure 12). The TTVs appear to have a sinusoidal period of about 475 days.

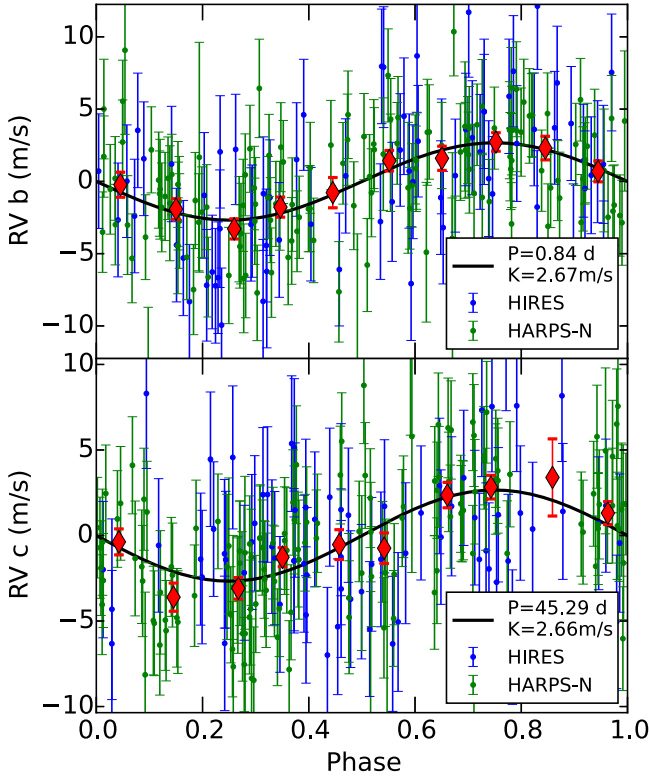


Figure 8. RVs from HIRES (blue) and HARPS-N (green) phase-folded to the periods of Kepler-10 b (top) and c (bottom). The red diamonds show the weighted mean RV of the HIRES and HARPS-N data combined in bins of 0.1 orbital phase. The best two-planet circular fit is shown in black. The orbits of both planets are constrained by the *Kepler*-determined transit times. The best two-planet circular fit yields $m_b = 3.72 \pm 0.42 M_{\oplus}$, and $m_c = 13.98 \pm 1.79 M_{\oplus}$.

Table 3
Two-planet Circular Fit MCMC Parameters

Parameter	Units	Median	+1 σ	-1 σ	References
HIRES jitter	m s^{-1}	3.62	0.41	0.37	A
HARPS jitter	m s^{-1}	2.49	0.24	0.21	A
γ	m s^{-1}	-0.01	0.23	0.23	A
Offset 1	m s^{-1}	0.44	0.63	0.64	A
Offset 2	m s^{-1}	-1.21	0.56	0.57	A
K_b	m s^{-1}	2.67	0.30	0.30	A
K_c	m s^{-1}	2.67	0.34	0.34	A
m_b	M_{\oplus}	3.72	0.42	0.42	A, B
m_c	M_{\oplus}	13.98	1.77	1.80	A, B
r_b	R_{\oplus}	1.47	0.03	0.02	B
r_c	R_{\oplus}	2.35	0.09	0.04	B
ρ_b	g cm^{-3}	6.46	0.72	0.74	A, B
ρ_c	g cm^{-3}	5.94	0.75	0.77	A, B

Note. All parameters were explored with uniform priors.

References. (A) This work. (B) Dumusque et al. (2014).

4.1. Measuring the Transit Times

From the photometry, we computed the TTVs twice. David Kipping measured the transit times TT_{Kip} , as documented in Kipping et al. (2015), and Eric Agol measured the transit times TT_{Agol} with the method described here. To include the impact of correlated noise on the transit timing uncertainty measured from the short cadence data, we carried out the following procedure: (1) We did a joint fit to the transits of both planets

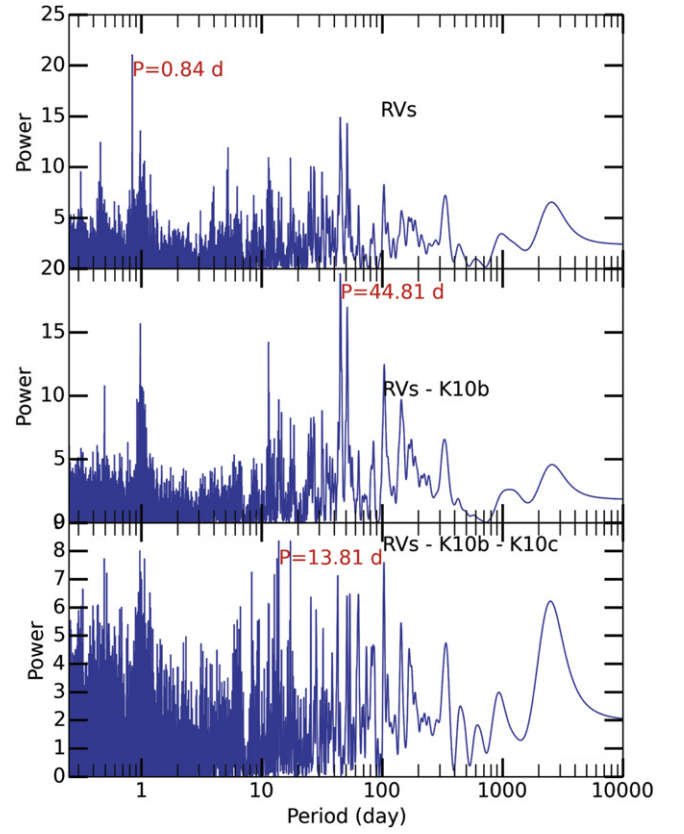


Figure 9. Top: L-S periodogram of the combined RVs from HIRES and HARPS-N. Center: L-S periodogram of the RVs after subtracting the model RVs for planet b. Bottom: L-S periodogram of the RVs after subtracting the model RVs for planets b and c.

assuming white noise and polynomial detrending near each transit. Overlapping transits of the two planets were modeled simultaneously. We let the transit times of 10 c vary, but fixed the transit times of 10 b to a periodic ephemeris. (2) We optimized this fit with a Levenberg–Marquardt model, and then subtracted it from the short cadence data. (3) We computed the autocovariance of the residuals to this initial fit for the short cadence light curve as a function of the number of cadences, $a(n)$, where $a(0)$ is the variance of the data and $a(1)$ is the covariance between residuals separated by one cadence, etc. We concatenated data across gaps when computing the autocovariance as these gaps are a small fraction of the entire dataset. (4) Using the computed autocovariance of the data, we computed the best-fit transit model to Kepler-10 c with the model for Kepler-10 b subtracted. We did not detrend at this stage, but instead used a covariance matrix computed from $a(n)$: $\Sigma_{i,j} = a(|i - j|)$.

The likelihood function was $\mathcal{L} \propto \exp\left(-\frac{1}{2}(\mathbf{r}^T \Sigma^{-1} \mathbf{r})\right)$, where \mathbf{r} is the residual vector for each transit after subtracting off the model component due to Kepler-10 b. We computed the timing uncertainties, $\sigma_{t,i}$, from the covariance of the model parameters at the best-fit value for the i th transit. We then allowed transit time to vary by $\pm 3\sigma_{t,i}$ for each transit, and mapped out the effective chi-square, $\chi^2 = -2 \ln \mathcal{L}$, versus timing offset. (5) We found the upper and lower time offsets at which the χ^2 of the fit changed by one, and chose the maximum of these offsets and $\sigma_{t,i}$ to estimate the transit timing uncertainty. The best-fit times of transit and the uncertainty are reported in Table 5.

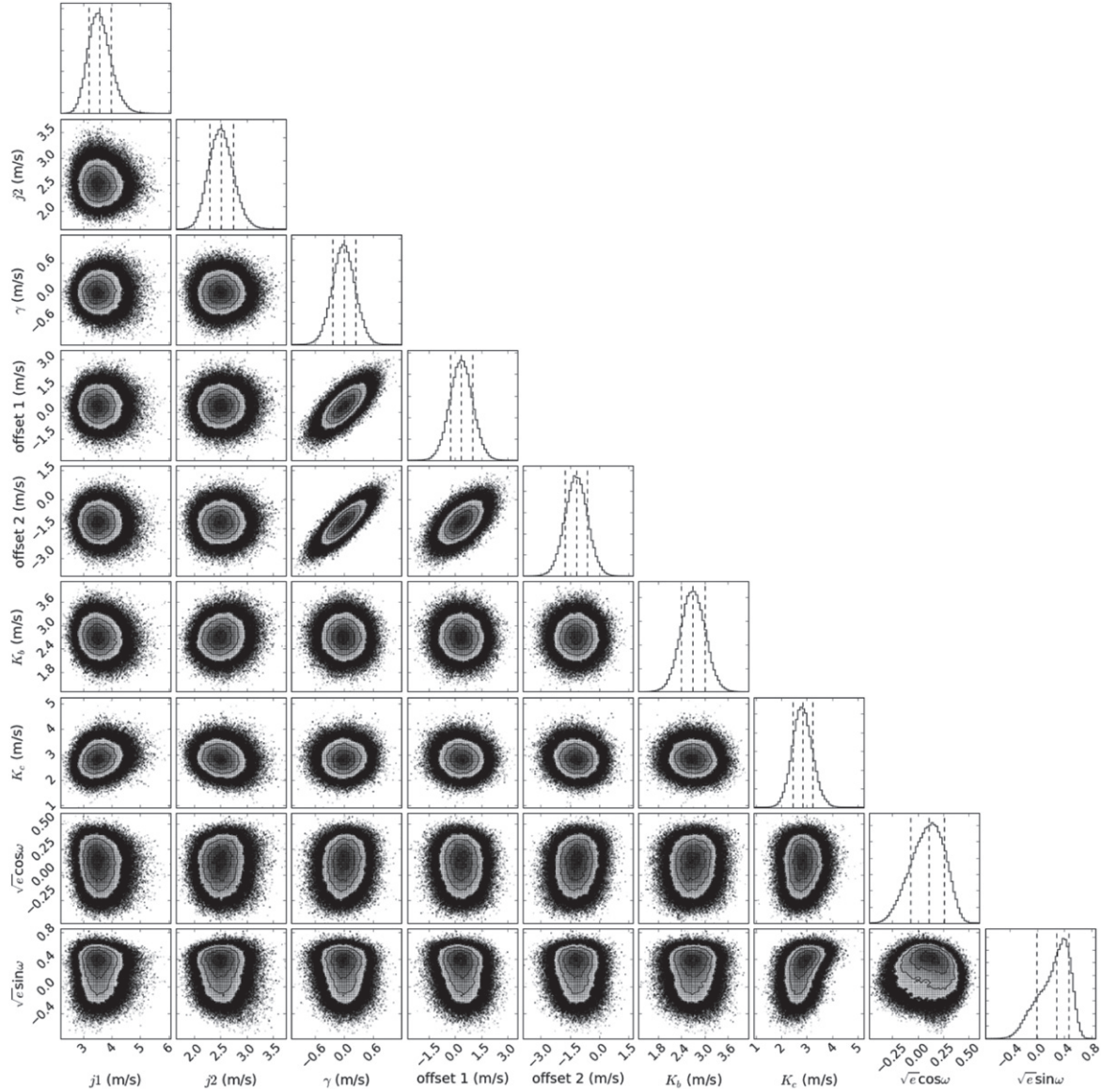


Figure 10. Posterior distribution for the two-planet fit to Kepler-10 RVs, allowing eccentricity for planet c. Variables are the jitter of the HIRES instrument (j_1), jitter of the HARPS-N instrument (j_2), velocity zero point (γ), velocity offset between HIRES and pre-upgrade HARPS-N RVs (offset 1), velocity offset between HIRES and post-upgrade HARPS-N RVs (offset 2), the semi-amplitudes of the RV curve for planets b (K_b) and c (K_c), and combinations of the eccentricity and argument of periastron of planet c, $\sqrt{e_c} \cos \omega_c$ and $\sqrt{e_c} \sin \omega_c$. The dashed lines indicate the 16th, 50th, and 84th percentiles.

5. FALSE ALARM PROBABILITY

We used two diagnostics to explore the possibility that the apparent coherent signal of the Kepler-10 c TTVs were due to noise, rather than planetary dynamics. First, we used a bootstrap test, which is a common method in the RV literature to assess whether an apparently coherent, sinusoidal signal could be produced by noise. Second, we used a Monte Carlo test. We applied each test to both TT_{AgoI} and TT_{Kip} .

5.1. Scramble (Bootstrap) Tests

We numbered the observed TTVs (O–C values) from 1– N and produced 10,000 fake data sets of length N . To construct each fake data set, we randomly drew a number j between 1 and N and used the j th observed transit as the first transit in our

fake data set. We repeated this procedure (including the possibility of drawing j again) until we had a fake data set of length N . Thus, it would be possible to draw j N times, or to draw each number between 1 and N exactly once, or any other combination from the N^N possibilities.

For each fake data set, we computed the Lomb–Scargle periodogram (Press & Rybicki 1989) of the fake TTVs from the Nyquist period (90.5 days, i.e., twice the orbital period of planet c) to 10,000 days. We found the period with the most power in the periodogram, and recorded this period (the “TTV super period”) and its associated power. We then compared the periodogram of the observations to our suite of 10,000 data sets (see Figure 13). By counting the number of fake data sets that produce a peak with more power than the observed peak, we can estimate the false alarm probability, i.e., the probability that

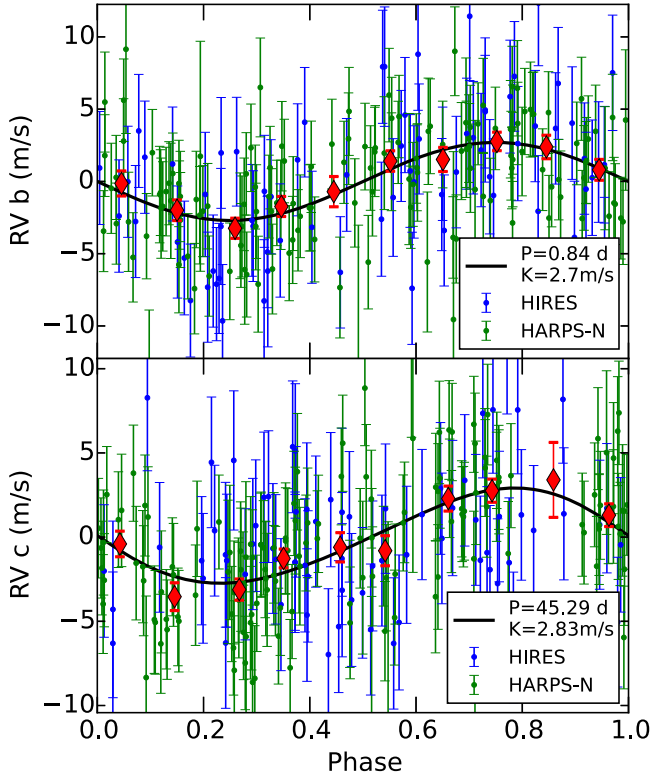


Figure 11. The RVs from HIRES (blue) and HARPS-N (green) phase-folded to the periods of Kepler-10 b (top) and c (bottom). The red diamonds show the weighted mean RV of the HIRES and HARPS-N data combined in bins of 0.1 orbital phase. The best two-planet fit in which the orbit of planet c ($P = 45.3$ day) is allowed to be eccentric is shown in black. The orbits of both planets are constrained by the *Kepler*-determined transit times. The best two-planet fit allowing eccentricity for planet c yields $m_b = 3.76 \pm 0.43 M_\oplus$, $m_c = 14.59 \pm 1.90 M_\oplus$, and $e_c = 0.17 \pm 0.13$.

Table 4
Two Planet Eccentric MCMC Parameters

Parameter	Units	Median	+1 σ	-1 σ	References
HIRES jitter	m s^{-1}	3.57	0.41	0.36	A
HARPS jitter	m s^{-1}	2.51	0.24	0.22	A
γ	m s^{-1}	-0.0	0.23	0.23	A
offset 1	m s^{-1}	0.35	0.64	0.64	A
offset 2	m s^{-1}	-1.17	0.57	0.57	A
K_b	m s^{-1}	2.7	0.31	0.31	A
K_c	m s^{-1}	2.83	0.4	0.37	A
$\sqrt{e} \cos \omega$...	0.11	0.16	0.18	A
$\sqrt{e} \sin \omega$...	0.29	0.18	0.29	A
e_c		0.13	0.12	0.09	A
ω_c	degree	66.81	31.19	68.51	A
m_b	M_\oplus	3.76	0.43	0.42	A, B
m_c	M_\oplus	14.59	1.93	1.87	A, B
r_b	R_\oplus	1.47	0.03	0.02	B
r_c	R_\oplus	2.35	0.09	0.04	B
ρ_b	g cm^{-3}	6.53	0.76	0.74	A, B
ρ_c	g cm^{-3}	6.21	0.82	0.8	A, B

Note. The priors on all the parameters were uniform.

References. (A) This work. (B) Dumusque et al. (2014).

noise, rather than an astrophysical signal, is responsible for the observed peak. For TT_{Agol} , we get $\text{FAP} = 3.89\%$. For TT_{Kip} , we get $\text{FAP} = 3.71\%$.

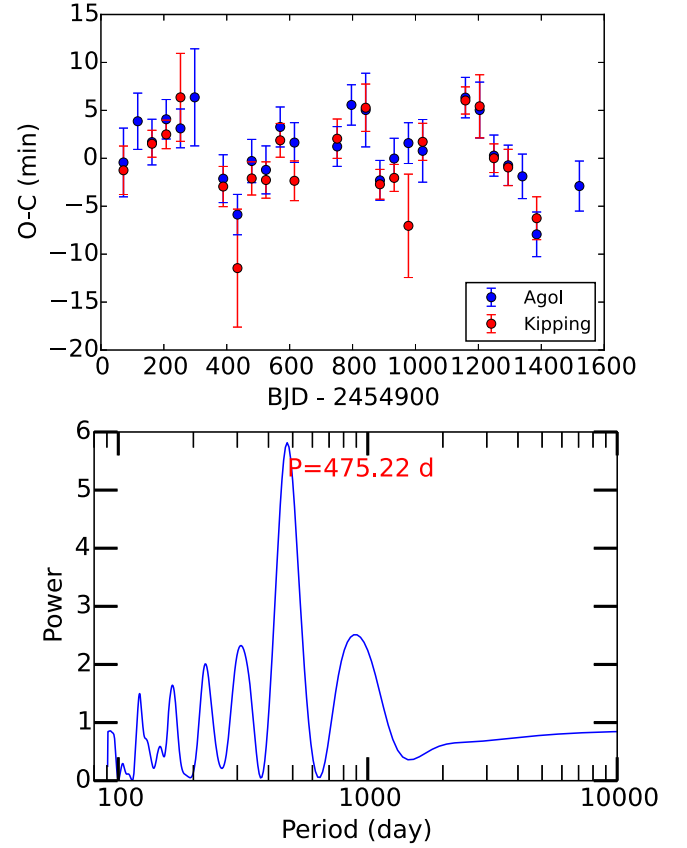


Figure 12. Top: the TTVs of Kepler-10 c measured in independent analyses by Eric Agol and David Kipping. The dependent axis (O-C) is the lateness of each observed transit with respect to a linear ephemeris. Bottom: the periodogram of Eric Agol's TTVs. The peak at 475 days corresponds to the observed sinusoidal period in the TTV time series and is the TTV super-period.

Table 5
Transit Times (TT_{Agol}) Measured from Short Cadence Transits of Kepler-10 c using a Correlated-noise Analysis

Transit	Time JD-2455000	Uncertainty (days)
0	62.2673	0.0017
1	107.5632	0.0014
2	152.8569	0.0014
3	198.1534	0.0436
4	288.7361	0.0014
5	334.0278	0.0015
6	379.3260	0.0016
7	424.6197	0.0016
8	469.9171	0.0014
9	515.2102	0.0014
10	651.0928	0.0014
11	696.3902	0.0015
12	741.6841	0.0015
13	786.9733	0.0014
14	832.2692	0.0015
15	877.5646	0.0015
16	922.8583	0.0015
17	1058.7451	0.0015
18	1104.0385	0.0016
19	1149.3295	0.0015
20	1194.6231	0.0015
21	1239.9166	0.0016
22	1285.2067	0.0016
23	1421.0931	0.0016

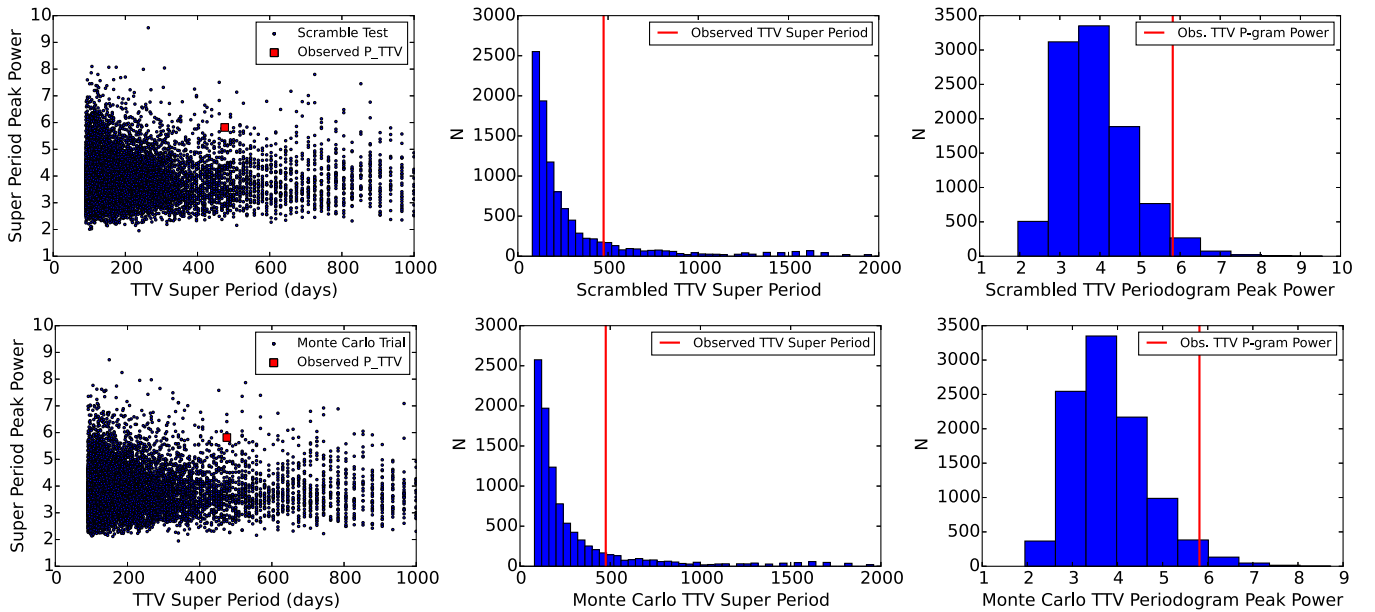


Figure 13. False alarm probability tests for the Kepler-10 TTVs. Top left: peak periodogram power as a function of TTV super-period for 10,000 scramble tests (black), as compared to the observed peak periodogram power and super-period. Top center: histogram of the super-periods generated from 10,000 scramble tests, compared to the observed TTV super-period. Top right: histogram of the peak periodogram powers generated from 10,000 scramble tests, compared to the observed peak periodogram power of the TTVs. Bottom row: same as top, but for 10,000 monte carlo tests.

5.2. Monte Carlo Tests

We generated 10,000 Monte Carlo fake data sets of transit midpoint times. To construct each fake data set, we drew a fake observation of each transit time from a Normal distribution with a mean of the observed transit time and a variance of the uncertainty in the transit time squared. We computed the false alarm probability in the same manner as for the scramble test, obtaining $\text{FAP} = 2.6\%$ for TT_{AgoI} , and $\text{FAP} = 1.89\%$ for TT_{Kip} (see Figure 13).

The FAP values of 1.9%–3.9% indicate a 3% probability that the apparent TTV super period is spurious and that the apparent coherence of the TTVs is a chance occurrence due to noise in the TTVs. This result differs from the Bayesian approach in Kipping et al. (2015), which finds the TTVs with 5σ confidence. Possible reasons for the difference between the FAP calculated in this work and the 5σ confidence found in Kipping et al. (2015) are (1) we look for a sinusoidal signal, whereas Kipping et al. (2015) look for any type of variation from a flat line, and (2) we ignore the error bars (since the errors in TT_{AgoI} are of nearly equal values), whereas Kipping et al. (2015) interpret the errors, allowing a few outliers with large errors to be down-weighted.

6. PLANETARY PROPERTIES OF KEPLER-10: THREE-PLANET SOLUTIONS

6.1. Analytical Motivation

If the observed coherent TTVs are due to the dynamical interactions of planets in the system, they indicate the presence of a third planet (KOI-72.X). Known planets (b and c) cannot cause the TTVs because planet c cannot be its own perturber, and planet b is too far away in period space ($P_c/P_b = 54$) to perturb planet c at the amplitude observed. Therefore, the best dynamical explanation of the TTVs is the existence of a third planet. The periodogram of the residual RVs after the RVs due to planets b and c are subtracted does not present a strong peak

(see Figure 9). Therefore we cannot unambiguously identify the orbital period KOI-72.X from the RVs alone.

We use analytic theory to predict the most likely orbital periods of a third planet. Equation (5) from Lithwick et al. (2012), also called the TTV equation, relates the super-period of the TTVs to the orbital periods of the two planets:

$$\frac{1}{P_{\text{TTV}}} = \left| \frac{j}{P} - \frac{j-1}{P'} \right| \quad (2)$$

where P_{TTV} is the super-period measured from the TTV sinusoid, P is the inner period, P' is the outer period, and the planets are near the $j:j-1$ resonance. Because the perturber can exist just inside or just outside the $j:j-1$ mean motion resonance, and because the perturber can be interior or exterior, there are 4 solutions for each $j:j-1$. Using Equation (2), we can predict a series of likely orbital periods for the perturber, planet candidate KOI-72.X, which are enumerated in Table 6.

6.2. Dynamical Solutions

For each candidate orbital period for KOI-72.X listed in Table 6, we perform a series of numerical N -body integrations using TTVFast (Deck et al. 2014). We use the analytically predicted orbital parameters as inputs to the integrator at epoch $T_0(\text{BJD} - 2454900) = 53.67844$. TTVFast predicts the times of transit of each planet in the N -body simulation, and the RVs of the star at the times of RV observation. To determine the orbital parameters that best reproduce the observed transit times and RVs, we minimize the following statistic:

$$\chi^2 = \sum_k \frac{(\text{TT}_{c,k} - \text{TT}_{c,\text{mod},k})^2}{\sigma_{\text{TT},c,k}^2} + \sum_i \frac{(\text{RV}_i - \text{RV}_{\text{mod},i})^2}{\sigma_{\text{RV},i}^2} \quad (3)$$

where the residuals between the observed and modeled transit times and RVs are simultaneously minimized. We fit the TTVs of only planet c, since planet b does not have significant,

Table 6
Using Equation (2), We Compute a Series of Likely Orbital Periods for Planet Candidate KOI-72.X

Analytic	Numerical—Parameters at Epoch $T_0 = 53.67844$ (BJD-2454900)														
$j:j-1$	P_X (predicted, days)	P_c (days)	P_X (days)	m_c (M_\oplus)	m_X (M_\oplus)	ecc_c	ω_c (degree)	ecc_X	ω_X (degree)	M_c (degree)	M_X (degree)	$\chi^2_{\text{TT},c}$	χ^2_{RV}	χ^2	ΔBIC^a
2:1	100	45.295	101.36	13.94	6.84	0.09	79.7	0.19	96.5	225.5	222.9	19	198	217	0.0
2:1	82.7	45.295	80.118	14.13	0.06	0.02	79.3	0.23	89.9	227.1	205.4	46	214	260	43.0
2:1	23.8	45.295	23.761	15.37	0.86	0.28	89.1	0.24	50.8	217.4	8.6	18	212	230	13.0
2:1	21.6	45.296	21.619	14.74	0.54	0.11	89.0	0.26	107.9	217.7	360.0	28	212	240	23.0
3:2	71.3	445.295	71.323	14.15	1.06	0.01	87.4	0.08	182.6	219.5	216.2	17	216	233	16.0
3:2	64.9	45.294	63.56	14.29	0.93	0.06	90.0	0.02	41.0	216.9	116.0	27	213	240	23.0
3:2	31.2	45.296	31.183	14.68	1.38	0.01	89.6	0.02	48.9	217.3	9.7	26	214	240	23.0
3:2	29.7	45.3	28.777	15.83	3.3	0.19	92.5	0.22	89.6	215.3	270.6	42	204	246	29.0
ctrl. 1 ^b	90.5	45.296	90.433	13.81	3.21	0.0	79.6	0.07	230.1	227.3	90.2	47	222	269	52.0
ctrl. 2 ^c	x	45.295	x	13.98	x	0.00	60.9	x	x	245.9	x	52	215	267	22.5

Notes. The left three columns show the analytic values that solve the TTV equation for the observed super-period of 475 days. The right columns show the parameters that minimize χ^2 between the observed TTVs and RVs and the N -body model. Each N -body model was seeded using the analytic prediction for KOI-72.X as an initial guess. The last two rows show control trials, in which (a) the initial orbital period of KOI-72.X is far from the analytic solutions to the TTV equation, and (b) there is no KOI-72.X.

^a The difference in the Bayesian Information Criterion (BIC) with respect to the best solution explored (at $P = 100$ days). According to Kass & Raftery (1995), the favorability for the model with the lower BIC value is “very strong” when $\Delta\text{BIC} > 10$, “strong” when $6 < \Delta\text{BIC} < 10$, “positive” when $2 < \Delta\text{BIC} < 6$, and “not worth more than a bare mention” when $0 < \Delta\text{BIC} < 2$.

^b KOI-72.X was placed exactly on the 2:1 exterior resonance, halfway between the 82 day and 101 day analytic solutions.

^c A two-planet dynamic solution with only Kepler-10 b and c (i.e., no KOI-72.X).

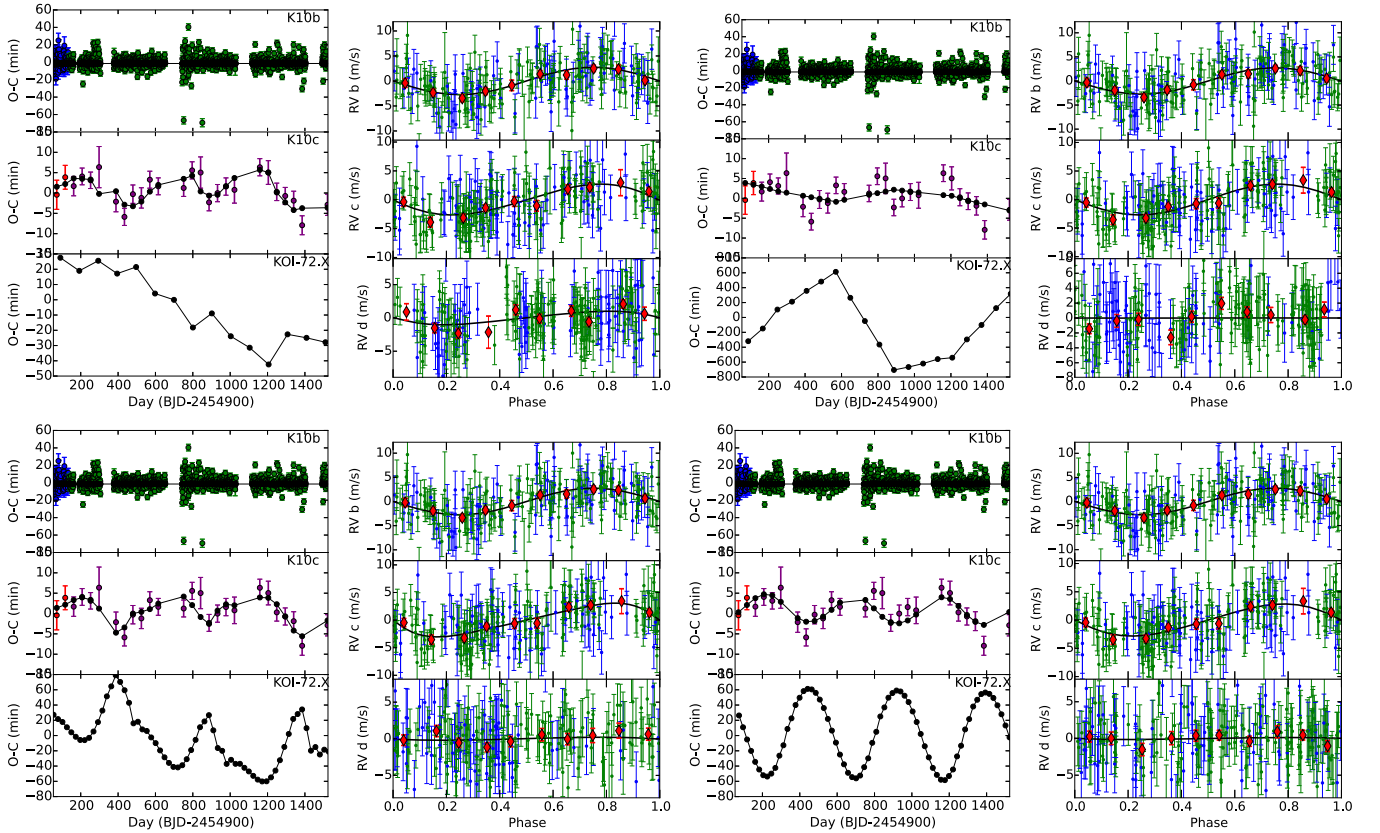


Figure 14. Solutions for KOI-72.X near the 2:1 mean motion resonance. Top left: O-C diagram for the solution with $P_X = 101$ days, showing the transit times of planets b, c, and X in the three vertical sub-panels. The colored points are the data; the black dotted line is the model. Top, second from left: RVs of Kepler-10 decomposed into the orbits of planets b, c, and d (top to bottom), where $P_X = 101$ days. The blue points are from HIRIS; the green are from HARPS-N, the red diamonds are the weighted mean RV in bins of 0.1 phase, and the black line is the model. Top, second from right, and top right: the same as the top left two panels, but for $P = 82$ days. Bottom left and second from the left: the same as top left two panels, but for $P = 23$ days. Bottom second from right, and right: the same as top left two panels, but for $P = 21$ days.

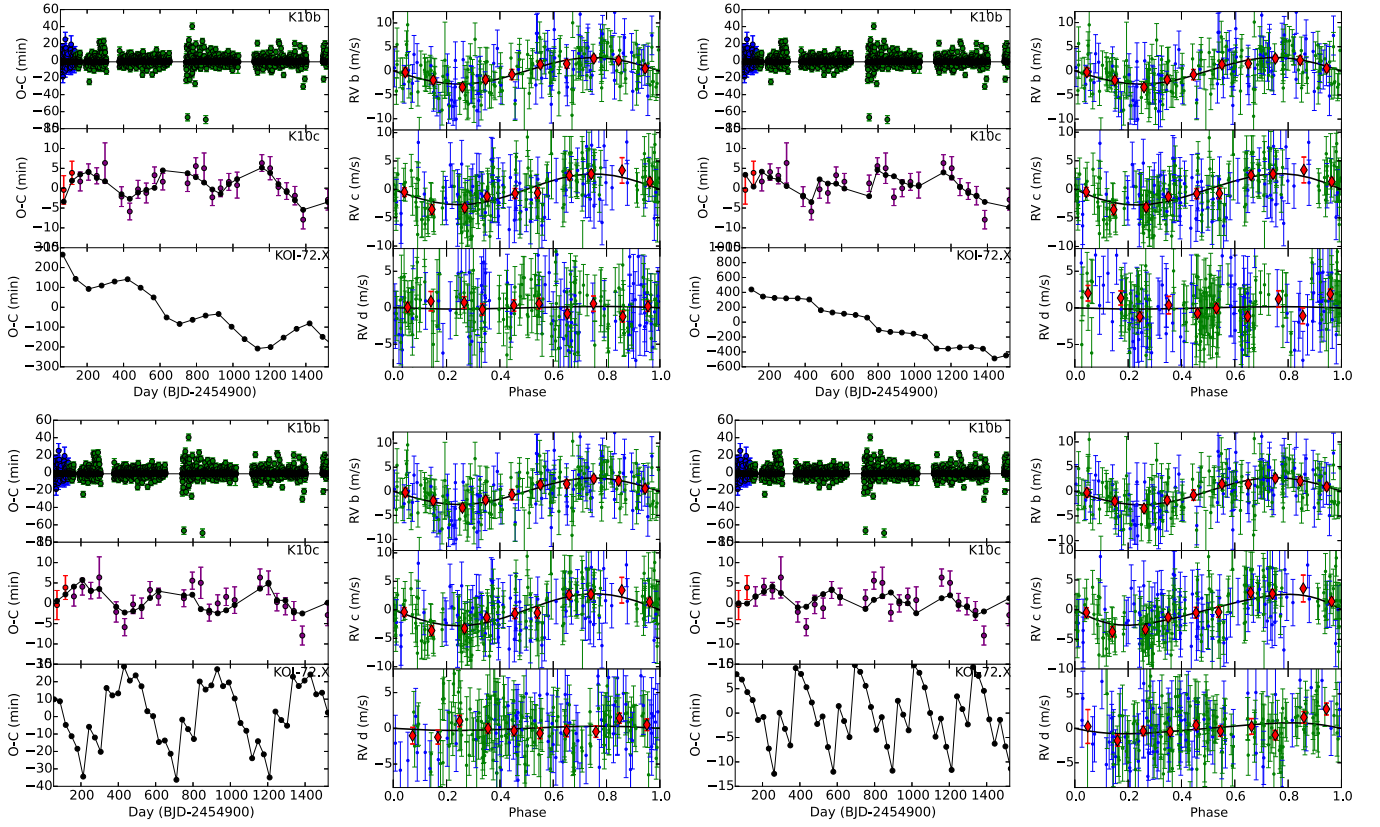


Figure 15. Solutions for KOI-72.X near the 3:2 mean motion resonance. The same as Figure 14 but with the top left two panels: $P_X = 71$ days; top right two panels: $P_X = 64$ days; bottom left two panels: $P_X = 31$ days; bottom right two panels: $P_X = 28$ days.

coherent TTVs. We use a combination of a Nelder–Mead and Levenberg–Marquardt (LM) minimization algorithm to find the orbital parameters and masses for planets c and d that produce a local minimum near the input orbital period. We allow the period (P), eccentricity (e), argument of periastron passage (ω), mean anomaly (M), and mass (m) of planets c and d to vary. We fix the inclination $i = 90^\circ$ and longitude of ascending node $\Omega = 0^\circ$ for all planets, for simplicity. The orbital parameters and mass of planet b are fixed, since planet b is not interacting with planet c or d. The outcome of the LM minimization for each input orbital period of KOI-72.X is listed in the right half of each row of Table 6. Figure 14 shows the numerical solutions in which KOI-72.X is near the 2:1 mean motion resonance. For each solution, the predicted TTVs are overlaid on the observed TTVs in the left panel, and the RVs are phase-folded to the orbits of each of the planets in the right panel. Figure 15 is the same, but for solutions in which KOI-72.X is near the 3:2 mean motion resonance.

Considering that there are 246 data points (26 transit times plus 220 RVs), the reduced χ^2 statistic is comparatively good for most of the orbital periods for KOI-72.X suggested by the TTV equation (top half of Table 6); however, we achieve $\chi^2_\nu \approx 1$ by construction based on how we treat the jitter in Equation (1). To convey how much some solutions are favored over others, we consider the change in the Bayesian Information Criterion (ΔBIC) as a way to rank the possible solutions in order of preference. The BIC is defined as:

$$\text{BIC} = \chi^2 + k \ln(n) \quad (4)$$

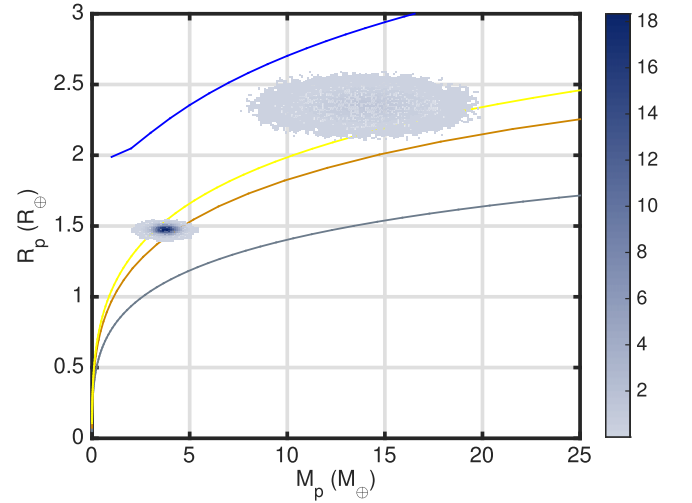


Figure 16. Mass-radius posterior distribution for Kepler-10 b and Kepler-10 c, compared to theoretical mass-radius relations. The color bar indicates the mass-radius posterior probability density conditioned on the combined HIRES and HARPS dataset. The solid curves represent theoretical mass-radius relations for notable compositions: pure Fe (gray), Earth-like stony-iron (brown), pure silicate (yellow), pure water (blue). The water planet mass-radius relation includes thermal effects and the presence of a super-critical steam envelope.

where k is the number of free parameters in the model and n is the number of observations (Schwarz 1978). The best solution for P_X is at 101 days ($\chi^2 = 217$). The ΔBIC between the best and second-best model is 13, meaning that our best solution

($P_X = 101$ days) is “very strongly favored” over all the other solutions (Kass & Raftery 1995). However, based on their low values of reduced $\chi^2 \approx 1$, the other solutions describe the data well enough that we cannot rule them out. Furthermore, the solutions listed above do not fully explore the high-dimensional parameter space. At each orbital period, multiple initial locations of KOI-72.X (as defined by ω_X , M_X , and e_X) are possible, and produce comparatively good χ^2 statistics to the values listed in Table 6. While the orbital solutions listed represent solutions that produce the lowest values of χ^2 found in our Nelder–Mead algorithm, the parameters ω_X , M_X , and e_X are poorly constrained by the TTVs and RVs, even when a particular orbital period for KOI-72.X is chosen. To fully explore the dynamical parameter space for the putative KOI-72.X would be very computationally intensive and is outside the scope of this paper.

Orbital periods for KOI-72.X that are not near solutions to the TTV equation produce significantly higher χ^2 values than orbital periods that solve the TTV equation. In the bottom half of Table 6, the “ctrl. 1” solution, we seed the orbital period for KOI-72.X with a value halfway between two solutions to the TTV equation ($P_X = 90.5$ days). Even after using the Nelder–Mead minimizer to find the best orbital parameters for planets c and d with this initial guess, the lowest value of χ^2 attained is 269, which is significantly worse (according to the BIC) than any of the analytically predicted solutions, with $\Delta\text{BIC} = 52$ (i.e., very strongly disfavored) with respect to the best three-planet solution. Thus, we numerically demonstrate that the TTV equation accurately predicts orbital periods for KOI-72.X that best reproduce the observed TTVs.

In the last row of Table 6 (“ctrl. 2”), we perform an N -body integration in which we simulate only planet b (which still has fixed orbital properties and a fixed mass) and planet c (for which the orbital parameters and mass are allowed to vary). The χ^2 statistic for this control test is 267 ($\Delta\text{BIC} = 22.5$), demonstrating that the best three-planet solution is strongly favored over the two-planet solution. In particular, the solutions for KOI-72.X at $P = 101$, 24, and 71 days achieve significantly lower BIC values than the two-planet model, suggesting that these orbital periods are strongly favored over a two-planet model.

The transit duration variations (TDVs) of Kepler-10 c are negligible. The various coplanar solutions for KOI-72.X that we examine all produce negligible TDVs as well, and so TDVs do not help break the degeneracy of the orbit for KOI-72.X in this particular system. The absence of TDVs implies that KOI-72.X is not highly inclined with respect to planets b and c.

The various dynamical solutions for KOI-72.X yield m_X between 1 and 7 M_\oplus . Without being able to choose the correct dynamical solution, we cannot pinpoint the mass of non-transiting planet candidate. However, the masses that best fit the TTVs and RVs are consistent with the population of low-mass, small planets discovered by *Kepler* and η -Earth surveys.

The family of solutions for KOI-72.X all yield similar masses for planet c (13.5–15 M_\oplus). This is likely because (1) the mass of KOI-72.X is small, meaning that it contributes little to the RVs, (2) planet c cannot create its own TTVs, and so the presence of TTVs should not be correlated with planet mass. For Kepler-10 c, modeling the TTVs with an N -body integrator does not result in an erroneously low planet mass.

7. INTERIOR STRUCTURE AND COMPOSITION OF KEPLER-10 b AND c

In this section, we estimate compositions of the planets Kepler-10 b and Kepler-10 c assuming the mass estimates from our formal fits using all available data. However, given the issues discussed in Section 2.3, actual uncertainties are larger than we assume for this analysis.

Kepler-10 c falls near the high density extreme among the locus of sub-Neptune-sized planet mass–radius measurements characterized to date. As such, Kepler-10 c presents a valuable test case for planet formation theories and interior structure models. Comparing measured masses and radii to theoretical mass–radius relations, which incorporate the behavior of materials at high pressure, reveals insights into the planets’ possible bulk compositions (Figure 16). We employ planet interior structure models from Rogers & Seager (2010a, 2010b), Rogers et al. (2011) to provide a mapping from planet mass and composition to radius, and apply the Bayesian approach described in Rogers & Seager (2010a) (and applied in Schmitt et al. 2014) to invert planet composition constraints from the RV and transit observations.

The first point to note about Kepler-10 c’s bulk composition is that its transit radius is likely not defined by a “rocky” or “solid” surface. In the vast majority (98.4%) of dynamical solutions to the combined *Kepler* photometry, HRES spectroscopy, and HARPS-N spectroscopy dataset, Kepler-10 c has a sufficiently low mean density (less dense than a pure magnesium silicate sphere) that the planet must have a substantial complement of volatiles (astrophysical ices and/or H/He) that contribute to the observed transit depth. Only 1.6% of the Kepler-10 c mass–radius posterior probability corresponds to scenarios in which the planet is sufficiently dense to have a stony-iron composition (comprised of an admixture iron and silicates alone). Since Kepler-10 c’s measured density necessitates that the planet contains a volatile complement that contributes to the transit depth, the planetary composition is inconsistent with a “solid” or “rocky” makeup.

The nature of Kepler-10 c’s volatiles is ambiguous; the planet could have a H/He envelope contributing less than a fraction of a percent by mass to the planet, or a water envelope contributing a few tens of percent of the planet mass. The measured mass and radius of Kepler-10 c are consistent with a “water-world” composition; less than 0.95% of the Kepler-10 c mass–radius posterior PDF spills into a low density regime wherein an H/He envelope is required (corresponding to planet configurations that are less dense than even a 100% pure water sphere with $T_{\text{eq}} = 550$ K). Assuming a 2-component planet interior structure model, where in the planet consists of an Earth-like stony-iron core (modeled as a 30:70 mix of iron and magnesium silicates) surrounded by a pure water envelope, the water mass fraction is constrained in this scenario to be $M_{\text{env,H}_2\text{O}}/M_p = 0.280^{+0.119}_{-0.102}$ (where the median, and range between the 16th and 84th percentiles are quoted) (Figure 17). At the other extreme, the measured mass and radius of Kepler-10 c are also consistent with a dry (water-less) mixture of stony-iron material and H/He. Coupling the planet mass–radius posterior distribution to a 2-component planet interior structure model wherein the planet consists of a Earth-like stony-iron core surrounded by a 30 times enhanced metallicity solar composition envelope, the H/He envelope mass fraction is constrained to be $M_{\text{env,H/He}}/M_p = 0.0023^{+0.0017}_{-0.0012}$ (Figure 18). Whether the planet’s volatile envelope is dominated by H/He

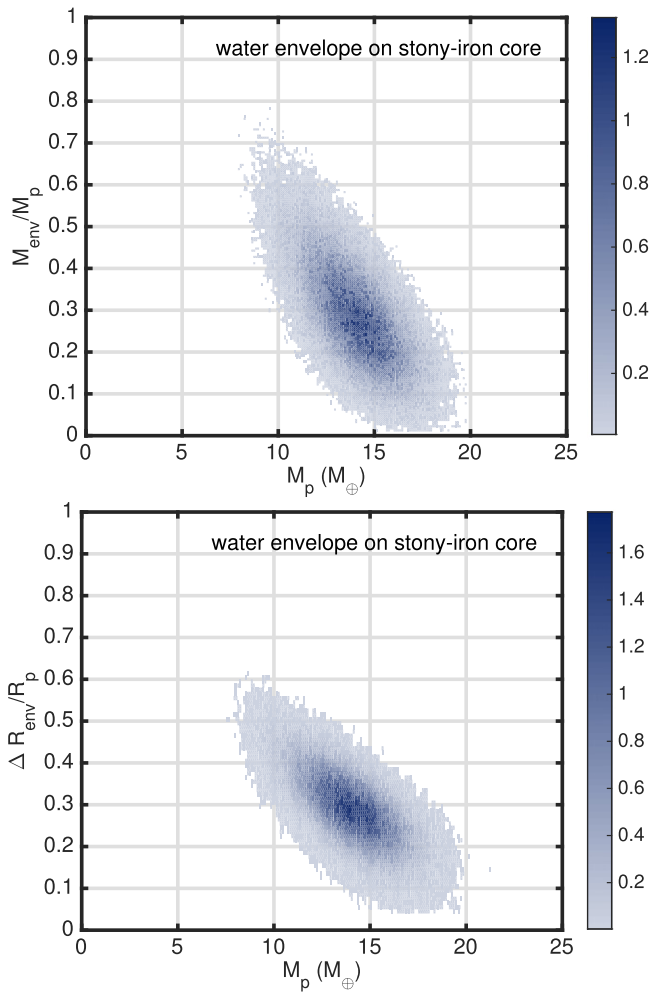


Figure 17. Posterior probability density distribution for Kepler-10 c, as a function of planet mass, M_p and the water envelope mass fraction $M_{\text{env,H}_2\text{O}}/M_p$ (upper panel), and radius fraction $R_{\text{env,H}_2\text{O}}/R_p$ (lower panel). Darker shades of blue represent higher probability. The posterior pdf obtained from the combined analysis of the Keck HIRES and HARPS-N radial velocity measurements is compared to planet interior structure models in which the planet is assumed to consist of an Earth-like stony-iron core (modeled as a 30:70 mix of iron and magnesium silicates) surrounded by a pure water envelope.

or water, the radial extent of the envelope, ΔR_{env} , accounts for more than one tenth of the planet radius; in the end member scenarios described above, $\Delta R_{\text{env,H}_2\text{O}}/R_p = 0.285^{+0.077}_{-0.073}$ and $\Delta R_{\text{env,HHe}}/R_p = 0.162^{+0.038}_{-0.037}$ (lower panels of Figures 17 and 18).

In contrast to Kepler-10 c, the measured mass and radius of the smaller inner planet, Kepler-10 b, is consistent with a rocky composition. Only 13.6% of the posterior probability of Kepler-10 b spills into a low-density regime of mass–radius parameter space where volatiles are demanded. Under the assumption of a 2-layer rocky planet model consisting of an iron core and a silicate mantle (having molar magnesium fraction $\text{Mg}\# = 90\%$), the iron core mass fraction of Kepler-10 b is constrained, $M_{\text{Fe,core}}/M_p = 0.169^{+0.115}_{-0.117}$ (Figure 19). The measured mass and radius of Kepler-10 b is consistent with an Earth-like bulk composition (32.5% iron core by mass), while an iron-enhanced Mercury composition (70% iron core by mass) is strongly disfavored.

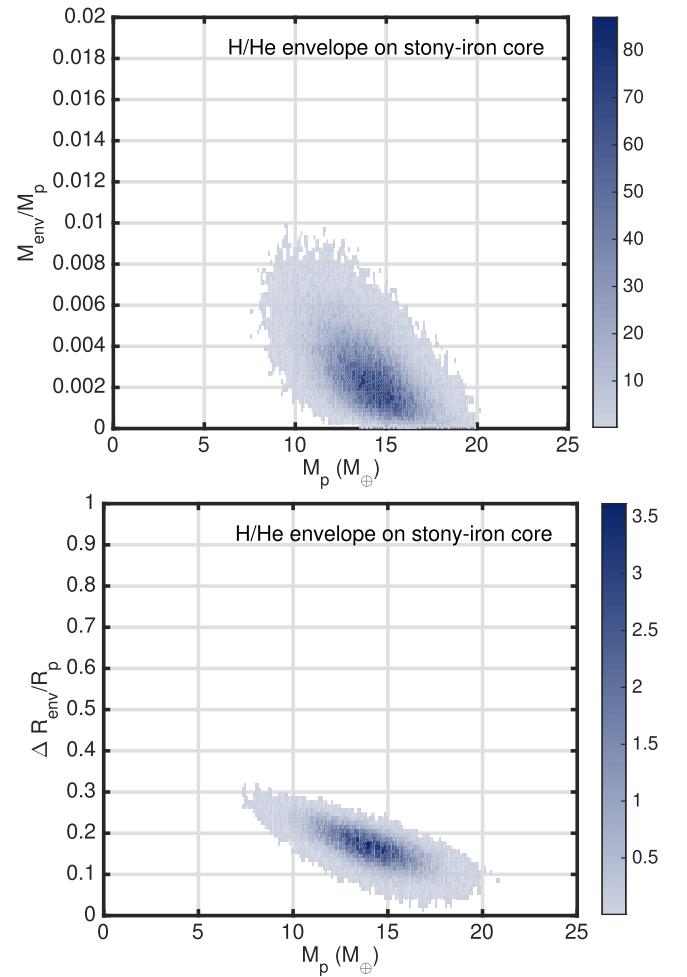


Figure 18. Posterior probability density distribution for Kepler-10 c, as a function of planet mass, M_p and the H/He envelope mass fraction $M_{\text{env,HHe}}/M_p$ (upper panel), and radius fraction $R_{\text{env,HHe}}/R_p$ (lower panel). This figure is analogous to Figure 17 except a H/He-dominated 30 times enhanced solar metallicity composition is assumed for the planet envelope instead of a pure water composition.

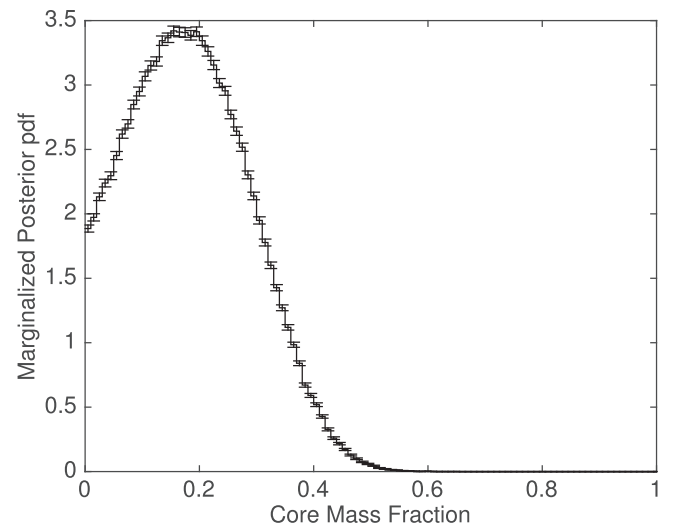


Figure 19. Posterior probability distribution on the iron core mass fraction of Kepler-10 b. A 2-layer fully differentiated interior structure model wherein the planet consists of an iron core surrounded by a silicate mantle ($\text{Mg}\# = 90\%$) is assumed.

All the composition constraints described above are based upon the combined analysis of the Keck HIRES and HARPS-N RV measurements. The qualitative constraints on Kepler-10 b and c's bulk compositions are largely unchanged when only the Keck HIRES RVs are used to derive the planet mass. Omission of the HARPS-N dataset from the analysis leads to a downward shift in the density of Kepler-10 c, an upward shift in the density of Kepler-10 b, and an overall broadening of all the posterior PDFs. The downward shift in the density of Kepler-10 c further strengthens the conclusion that Kepler-10 c has a volatile envelope. Conditioned on the HIRES data alone, there is only a 0.4% posterior probability that Kepler-10 c is more dense than a pure silicate sphere (compared to 4.1% conditioned on both HARPS-N and HIRES). Further, the posterior probability that Kepler-10 c is sufficiently dense to have water envelope (instead of H/He) also decreases to 62% (compared to 99% conditioned on both HARPS-N and HIRES). On the other hand, the shift in Kepler-10 b posterior distribution toward higher masses and densities leads to increased posterior probability at higher Kepler-10 b iron core mass fractions $M_{\text{Fe,core}}/M_p = 0.44^{+0.15}_{-0.19}$ (compared to 0.17 ± 0.12 based on both HARPS-N and HIRES).

8. DISCUSSION

8.1. Insights on Successful Observing Strategies for Kepler Follow-up

The source of the discrepancy between the HIRES and HARPS-N RVs is unknown. However, the apparent time-variability of K_b and K_c on both instruments suggests that a time-correlated noise (or astrophysical signal) confounds both data sets on timescales of a summer observing season. This time-correlated property could be from stellar rotation and the stellar magnetic cycle or from an additional planet in the system. The most effective way to combat this time-correlated noise is to increase the quantity and baseline of observations of this star. This strategy of employing a long observing baseline compared to time-correlated noise influences should be employed on other stars with low-mass planets to avoid confusion in the future.

8.2. The Masses and Densities of the Kepler-10 Planets

This paper is the third study of the masses and densities of the Kepler-10 planets. B11 and D14 previously measured the planetary and stellar properties of the Kepler-10 system. The stellar and planetary parameters they found are shown in Table 7. The planetary properties obtained in this paper are also shown. We include our solutions to the two-planet circular fit, the two-planet fit in which planet c is allowed eccentricity, and the best three-planet fit.

Table 7 reveals how the estimates of the masses of Kepler-10 b and c have changed based on which RVs were included in the analysis. B11 used 52 RVs from Keck HIRES that were timed at the quadratures of planet b, and spanned 2 seasons (2009–2010). They assumed that both planets had circular orbits. They obtained masses of $m_b = 4.56 \pm 1.23 M_\oplus$, and an upper limit for planet c, $m_c < 20 M_\oplus$. D14 used 148 RVs from TNG HARPS-N that were timed at the quadratures of planet c, and spanned 2 seasons (2012–2013). They assumed that both planets had circular orbits. They obtained $m_b = 3.3 \pm 0.49 M_\oplus$, a measurement 1σ lower than the B11 mass for Kepler-10 b, and a mass measurement for planet c of

$m_c = 17.2 \pm 1.9 M_\oplus$. Analyzing the 52 literature RVs plus 20 new RVs from HIRES, we obtain $m_b = 4.61 \pm 0.83 M_\oplus$ and $m_c = 5.69^{+3.19}_{-2.90} M_\oplus$, which are 1.1σ and 3.1σ away from the values in D14, respectively. We combine the 72 RVs from HIRES with 148 literature RVs from HARPS-N to obtain the best orbital coverage of both planets and the longest baseline. In our two-planet circular fit (the most direct orbital comparison to the previous studies), we obtain $m_b = 3.72 \pm 0.42 M_\oplus$ and $m_c = 13.98 \pm 1.79 M_\oplus$. The mass we obtain for Kepler-10 b sits between the two previously published values. Likewise, the mass we obtain for Kepler-10 c represents a compromise between the 2σ detection in the HIRES data and the massive planet obtained in the HARPS-N data.

When we allow the orbit of Kepler-10 c to be eccentric, or when we add a third planet to the system, the mass of Kepler-10 c does not change significantly. The mass for Kepler-10 c obtained in the eccentric fit ($m_c = 14.59 \pm 1.90 M_\oplus$) is consistent with our circular fit. Likewise, the masses for planet c obtained for various orbital solutions of candidate KOI-72.X all resulted in $m_c = 13\text{--}14.5 M_\oplus$; i.e., all within 1σ of the mass we obtained in the two-planet circular fit. Therefore, allowing the orbit of planet c to be eccentric, or including a third planet at a variety of orbital periods, does not significantly affect the mass computed for Kepler-10 c.

8.3. Updated Mass–Radius and Density–Radius Relations

We incorporate our newly derived mass measurements of the Kepler-10 planets, as well as several new planet discoveries, in an updated mass–radius relation. The planets are the same as those in Weiss & Marcy (2014), with the inclusion of planets listed in Table 8. Figure 20 shows how the weighted mean density and weighted mean mass of planets changes from 0 to 4 Earth radii.

Figure 20 shows where Kepler-10 b and c sit in the density–radius and mass–radius diagrams for planets smaller than $4 R_\oplus$. As one of the first rocky exoplanet discoveries, Kepler-10 b has shaped our expectations for rocky exoplanets. Like Kepler-10 b, most of the rocky exoplanets discovered so far are larger than the Earth. This is because larger planets are easier to detect in transit, and because the masses of large, rocky planets are easier to measure than the masses of small, possibly rocky planets.

Kepler-10 b, at $1.47 R_\oplus$, sits very close to the peak of the density–radius diagram (at $1.5 R_\oplus$). Planet density increases with planet radius for $R_p < 1.5 R_\oplus$, not only in the solar system terrestrial planets, but also among the few exoplanets with measured masses in this radius range (Kepler-78 b, Kepler-10 b, Kepler-36 b, Corot-7 b, Kepler-93 b). We attribute the empirical linear increase in planet density with radius to the slight compressibility of rock. The density of rock changes gradually with increasing planet mass or radius, and so the first-order (linear) Taylor expansion of the true density–radius relation of rock is sufficient to describe the observed terrestrial planets and exoplanets smaller than $1.5 R_\oplus$. Kepler-10 b ($R_p = 1.47 R_\oplus$, $\rho_p = 6.68 \text{ g cm}^{-3}$) sits exactly on the linear density–radius relation that describes the terrestrial planets. Kepler-10 b also achieves a density consistent with an Earth-like composition (67.5% MgSiO_3 , 32.5% Fe, Seager et al. 2007).

Kepler-10 c, at $2.35 R_\oplus$, sits to the right of the peak of the density–radius diagram. Its density (5.74 g cm^{-3}) is among the highest for planets between 2.0 and $2.5 R_\oplus$. However, its

Table 7
Kepler-10 Parameters in Different Studies

Parameter	Units	B11 ^a	D14 ^b	This Work HIRES only	2 pl. circ.	2 pl. ecc.	Best 3 pl.
Stellar							
T_{eff}	K	5627 ± 44	5708 ± 28	same as D14			
$\log g$	cgs	4.341 ± 0.012	4.344 ± 0.004
M_*	M_{\odot}	0.895 ± 0.060	0.910 ± 0.0214
R_*	R_{\odot}	1.056 ± 0.021	1.065 ± 0.009
L_*	L_{\odot}	1.004 ± 0.059	1.004 ± 0.059
[Fe/H]	dex	-0.15 ± 0.04	-0.15 ± 0.04
$v \sin i$	m s^{-1}	0.5 ± 0.5	$0.6 \pm 0.5-2.04 \pm 0.34$
Age	Gyr	11.9 ± 4.5	10.6 ± 1.4
Kepler-10 b							
Period	days	$0.837495 \pm 4\text{E-}6$	$0.8374907 \pm 2\text{E-}7$	fixed, same as D14			
TT	BJD—2,454,900	64.57375 ± 0.0007	134.08687 ± 0.00018	fixed, same as D14			
K	m s^{-1}	3.3 ± 0.9	2.38 ± 0.35	3.31 ± 0.59	2.67 ± 0.3	2.70 ± 0.31	2.67 (fixed)
a	AU	0.01684 ± 0.00033	0.01685 ± 0.00013	fixed, same as D14			
M_p	M_{\oplus}	4.56 ± 1.23	3.33 ± 0.49	4.61 ± 0.83	3.72 ± 0.42	$3.76 \pm 0.43 M_{\oplus}$	3.70 (fixed)
R_p	R_{\oplus}	1.416 ± 0.034	1.47 ± 0.03	fixed, same as D14			
ρ_p	g cm^{-3}	8.8 ± 2.5	5.8 ± 0.8	8.0 ± 1.43	6.46 ± 0.72	6.53 ± 0.75	6.46 (fixed)
Kepler-10 c							
Period	days	45.29485 ± 0.0007	$45.294301 \pm 4.8\text{E-}5$	fixed, same as D14			45.295
TT	BJD-2454900	71.6761 ± 0.0022	162.26648 ± 0.00081	fixed, same as D14			71.67
K	m s^{-1}	x	3.26 ± 0.36	1.09 ± 0.58	2.67 ± 0.34	2.83 ± 0.38	2.66
a	AU	0.2407 ± 0.0048	0.2410 ± 0.0019	fixed, same as D14			0.24
e		0 (fixed)	0 (fixed)	0 (fixed)	0 (fixed)	0.17 ± 0.13	0.09
ω_c	°	71 ± 20	79.7
M_p	M_{\oplus}	<20	17.2 ± 1.9	$5.69^{+3.19}_{-2.90}$	13.98 ± 1.79	14.59 ± 1.90	13.94
R_p	R_{\oplus}	2.277 ± 0.054	2.35 ± 0.06	fixed, same as D14			
ρ_p	g cm^{-3}	<10	7.1 ± 1.0	$2.42^{+1.36}_{-1.24}$	5.94 ± 0.75	6.21 ± 0.81	6.20
KOI-72.X							
Period	days	101.360 ^c
e		0.19 ^c
M_p	M_{\oplus}	6.84 ^c

Notes.^a B11—Batalha et al. (2011).^b D14—Dumusque et al. (2014).^c The variety of orbital solutions with similar goodness of fit for planet candidate KOI-72.X prevents an accurate characterization of the planet's true orbital parameters and mass. The numbers shown here reflect the best three-planet solution, which is strongly preferred over the two-planet solution and over other three-planet solutions based on the BIC.

Table 8
Planetary Mass and Radius Measurements from 2014 to 2015

Name	Period (day)	Mass (M_{\oplus})	Radius (R_{\oplus})	Insolation (S_{\oplus})	First References	Orbital References
Kepler-138 b	10.3126	0.066 ± 0.048	0.522 ± 0.032	6.90	Borucki et al. (2011)	Jontof-Hutter et al. (2015)
Kepler-138 c	13.7813	1.97 ± 1.5	1.197 ± 0.070	4.75	Borucki et al. (2011)	Jontof-Hutter et al. (2015)
Kepler-138 d	23.0881	0.640 ± 0.520	1.212 ± 0.075	2.35	Borucki et al. (2011)	Jontof-Hutter et al. (2015)
HIP 116454 b	9.120500	11.82 ± 1.33	2.530 ± 0.180	43.2	Vanderburg et al. (2015)	Vanderburg et al. (2015)
Kepler-93 b	4.726740	4.02 ± 0.68	1.478 ± 0.019	278	Borucki et al. (2011)	Dressing et al. (2015)
KOI-273 b	10.600000	5.46 ± 2.50	1.820 ± 0.100	119	Borucki et al. (2011)	Gettel et al. (2016)
Wasp-47 e	0.789597	<22	1.829 ± 0.070	3998	Becker et al. (2015)	Becker et al. (2015)
Wasp-47 d	9.03081	15.2 ± 7	3.63 ± 0.14	155	Becker et al. (2015)	Becker et al. (2015)

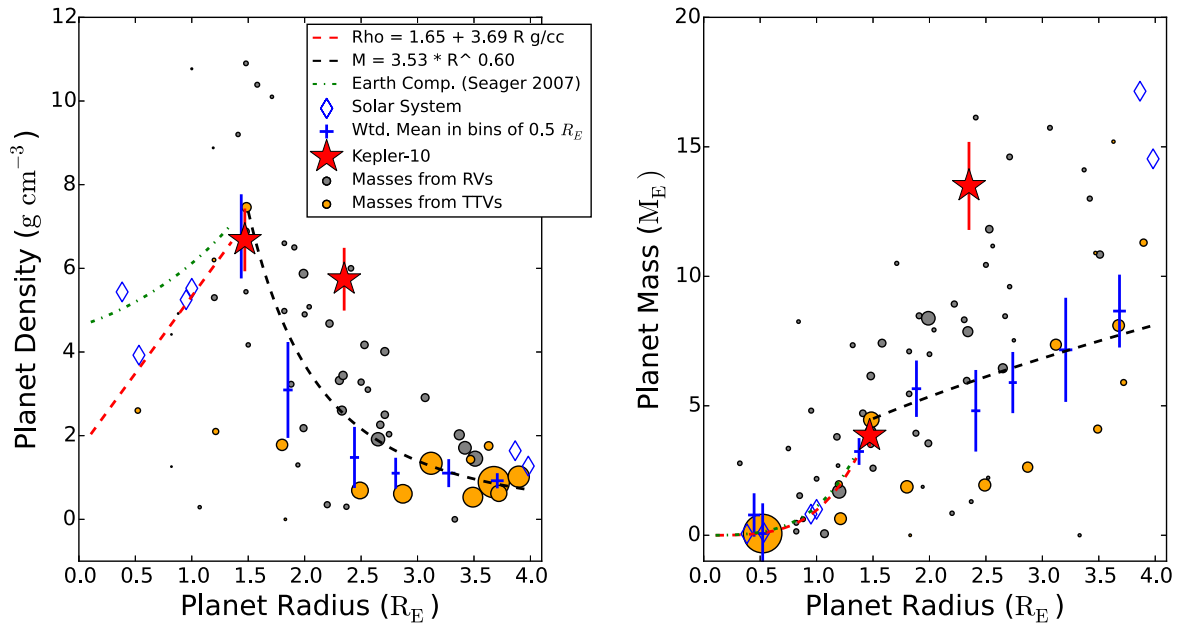


Figure 20. Left: planet density as a function of planet radius for planets smaller than $4 R_{\oplus}$, updated from Weiss & Marcy (2014). Planets with mass measurements from RVs are in gray; planets with mass measurements from TTVs are in gold. The size of the dot corresponds to $1/\sigma_m^2$. Kepler-10 b and c are shown as large red stars. The solar system planets are shown as blue diamonds. The blue crosses show the weighted mean density in bins of $0.5 R_{\oplus}$ to guide the eye, and their vertical error bars represent the rms scatter of planet densities in that bin. The green line is the predicted bulk density for a 32.5% Fe, 67.5% MgSiO_3 planet (like Earth) as a function of radius (Seager et al. 2007). The red line is an empirical linear fit to planet density as a function of radius for $R_p < 1.5 R_{\oplus}$. The black line is an empirical power law fit to planet mass as a function of radius for $R_p > 1.5 R_{\oplus}$. Right: planet mass as a function of planet radius for $R_p < 4 R_{\oplus}$. The symbols and lines are the same as to the left, but the sizes of the dots corresponds to $1/\sigma_m^2$.

density is still lower than the density of Kepler-10 b. Neither the empirical density–radius relation for rocky planets, nor the Seager et al. (2007) prediction for the densities of rocky planets, intersects with Kepler-10 c’s position on the mass–radius diagram. Extrapolating from both of these relations, we would expect the density of a $2.35 R_{\oplus}$ Earth-composition planet to be 11 g cm^{-3} , nearly twice the observed density for Kepler-10 c. The mass and radius of Kepler-10 c are inconsistent with a stony-iron planet.

Composition modeling for Kepler-10 c strongly disfavors a rocky interpretation. Less than 2% of the posterior distribution on the planet’s mass and radius permits a planet denser than pure perovskite. A stony-iron composition like the Earth and other known rocky exoplanets is excluded with high confidence. Kepler-10 c may have a stony-iron interior overlaid with a 0.2% mass (16% radius) hydrogen–helium envelope. Alternatively, Kepler-10 c may be a stony-iron interior covered with super-ionic water and a steam envelope.

Planet candidate KOI-72.X cannot be shown on the mass–radius diagram because it does not transit, and so its radius cannot be measured.

9. CONCLUSIONS

In this paper, we present the revised masses and densities of Kepler-10 b and c based on 220 RVs from two telescopes, 1.5 times as many RVs as were used in the most recent analysis of this planetary system. The combined RVs yield a baseline 3 times as long as any previous RV publication for this system. We find Kepler-10 b has $m_b = 3.72 \pm 0.42 M_{\oplus}$ and $\rho_b = 6.46 \pm 0.73 \text{ g cm}^{-3}$, and Kepler-10 c has $m_c = 13.98 \pm 1.79 M_{\oplus}$ and $\rho_c = 5.94 \pm 0.76 \text{ g cm}^{-3}$. However, we note that analysis of only HARPS data yields a higher mass for planet b and a lower mass for planet c than

does analysis of the HARPS-N data alone, with the mass estimates for Kepler-10 c being formally inconsistent at the 3σ level. While we cannot identify the source of the disagreement between the HARPS and HARPS-N RVs, we note that the apparent time-variability of K_b and K_c in both instruments suggests that time-correlated noise, in the form of either stellar activity or an additional planet, is responsible for the apparent discrepancy. The time-correlated noise indicates that the uncertainties in the masses of the planets (especially planet c) likely exceed our formal estimates. More RVs and/or better priors on the stellar rotation period are needed to adequately model the time-correlated noise without compromising our analysis of the planetary signal of Kepler-10 c. We jointly analyze the TTVs and RVs of the Kepler-10 system to find planet candidate KOI-72.X. Several possible orbital solutions exist for KOI-72.X, with orbital periods ranging from 21–100 days, and masses ranging from 1 to $7 M_{\oplus}$. The existence of KOI-72.X has a negligible effect on the mass solutions for Kepler-10 b and Kepler-10 c.

9.1. Compositions of Kepler-10 b and Kepler-10 c

Kepler-10 b is very likely a planet with a rocky surface. Its density is consistent with a stony-iron composition (90.8% of the posterior distribution is denser than MgSiO_3). Assuming a 2-layer model with an iron core and silicate mantle, the iron core mass fraction of Kepler-10 b is constrained at 0.17 ± 0.12 . Kepler-10 c is inconsistent with a purely rocky composition (only 1.6% of its posterior distribution is denser than pure MgSiO_3). Kepler-10 c may be a stony-iron interior overlaid with a 0.2% mass (16% radius) hydrogen–helium envelope. Alternatively, Kepler-10 c may be a stony-iron interior covered with a 28% mass (29% radius) super-ionic water envelope.

9.2. Non-transiting Planet Candidate KOI-72.X

From the coherent TTVs of Kepler-10 c, we identify a third, non-transiting planet candidate KOI-72.X. There is a 3% probability that the coherent TTVs are due to noise rather than a third planet. We explore possible solutions for the third planet, especially solutions that satisfy the TTV equation for the observed super-period of the TTVs, by running numerical N -body simulations over the duration of the *Kepler* observations. We demonstrate that orbital periods for the third planet that satisfy the TTV equation better reproduce the observed TTVs than other orbital periods do. Some orbital solutions for the third planet are interior to Kepler-10 c, while others are exterior. The most likely orbital periods for the non-transiting planet are 101 days, 24 days, and 71 days, which are near the 2:1, 1:2, or 3:2 mean motion resonance with planet c. The mass for the non-transiting planet candidate ranges from 1 to $7 M_{\oplus}$.

LMW gratefully acknowledges support from Kenneth and Gloria Levy. This research was supported in part by the National Science Foundation under Grant No. NSF PHY11-25915 via the Dynamics of Exoplanets workshop at the Kavli Institute for Theoretical Physics in Santa Barbara, CA. We thank Tsevi Mazeh for informative discussions regarding time-correlated noise. The authors wish to extend special thanks to those of Hawaiian ancestry on whose sacred mountain of Maunakea we are privileged to be guests. Without their generous hospitality, the Keck observations presented herein would not have been possible.

REFERENCES

- Batalha, N. M., Borucki, W. J., Bryson, S. T., et al. 2011, *ApJ*, **729**, 27
- Batalha, N. M., Rowe, J. F., Bryson, S. T., et al. 2013, *ApJS*, **204**, 24
- Becker, J. C., Vanderburg, A., Adams, F. C., Rappaport, S. A., & Schwengeler, H. M. 2015, *ApJL*, **812**, L18
- Borucki, W. J., Koch, D. G., Basri, G., et al. 2011, *ApJ*, **736**, 19
- Bruntt, H., Deleuil, M., Fridlund, M., et al. 2010, *A&A*, **519**, A51
- Burke, C. J., Bryson, S. T., Mullally, F., et al. 2014, *ApJS*, **210**, 19
- Butler, R. P., Marcy, G. W., Williams, E., McCarthy, C., & Vogt, S. S. 1996, *PASP*, **108**, 500
- Carter, J. A., Agol, E., Chaplin, W. J., et al. 2012, *Sci*, **337**, 556
- Dawson, R. I., & Fabrycky, D. C. 2010, *ApJ*, **722**, 937
- Deck, K. M., Agol, E., Holman, M. J., & Nesvorný, D. 2014, *ApJ*, **787**, 132
- Dragomir, D., Matthews, J. M., Eastman, J. D., et al. 2013, *ApJL*, **772**, L2
- Dressing, C. D., et al. 2015, *ApJ*, **800**, 135
- Dumusque, X., Bonomo, A. S., Haywood, R. D., et al. 2014, *ApJ*, **789**, 154
- Foreman-Mackey, D., Hogg, D. W., Lang, D., & Goodman, J. 2013, *PASP*, **125**, 306
- Fressin, F., Torres, G., Charbonneau, D., et al. 2013, *ApJ*, **766**, 81
- Fressin, F., Torres, G., Desert, J.-M., et al. 2011, *ApJS*, **197**, 5
- Gettel, S., Charbonneau, D., Dressing, C. D., et al. 2016, *ApJ*, **816**, 95
- Gilliland, R. L., Marcy, G. W., Rowe, J. F., et al. 2013, *ApJ*, **766**, 40
- Grunblatt, S. K., Howard, A. W., & Haywood, R. D. 2015, *ApJ*, **808**, 127
- Haywood, R. D., Collier Cameron, A., Queloz, D., et al. 2014, *MNRAS*, **443**, 2517
- Howard, A. W., Johnson, J. A., Marcy, G. W., et al. 2010, *ApJ*, **721**, 1467
- Howard, A. W., Johnson, J. A., Marcy, G. W., et al. 2011a, *ApJ*, **726**, 73
- Howard, A. W., Johnson, J. A., Marcy, G. W., et al. 2011b, *ApJ*, **730**, 10
- Howard, A. W., Sanchis-Ojeda, R., Marcy, G. W., et al. 2013, *Natur*, **503**, 381
- Jontof-Hutter, D., Lissauer, J. J., Rowe, J. F., & Fabrycky, D. C. 2014, *ApJ*, **785**, 15
- Jontof-Hutter, D., Rowe, J. F., Lissauer, J. J., Fabrycky, D. C., & Ford, E. B. 2015, *Natur*, **522**, 321
- Kass, R. E., & Raftery, A. E. 1995, *J. Am. Stat. Assoc.*, **90**, 773
- Kipping, D. M., Nesvorný, D., Buchhave, L. A., et al. 2014, *ApJ*, **784**, 28
- Kipping, D. M., Schmitt, A. R., Huang, X., et al. 2015, *ApJ*, **813**, 14
- Lissauer, J. J., Fabrycky, D. C., Ford, E. B., et al. 2011, *Natur*, **470**, 53
- Lissauer, J. J., Jontof-Hutter, D., Rowe, J. F., et al. 2013, *ApJ*, **770**, 131
- Lissauer, J. J., Marcy, G. W., Rowe, J. F., et al. 2012, *ApJ*, **750**, 112
- Lithwick, Y., Xie, J., & Wu, Y. 2012, *ApJ*, **761**, 122
- Marcy, G. W., Isaacson, H., Howard, A. W., et al. 2014, *ApJS*, **210**, 20
- Mullally, F., Coughlin, J. L., Thompson, S. E., et al. 2015, *ApJS*, **217**, 31
- Pepe, F., Cameron, A. C., Latham, D. W., et al. 2013, *Natur*, **503**, 377
- Petigura, E. A., Howard, A. W., & Marcy, G. W. 2013a, *PNAS*, **110**, 19273
- Petigura, E. A., Marcy, G. W., & Howard, A. W. 2013b, *ApJ*, **770**, 69
- Press, W., & Rybicki, G. 1989, *ApJ*, **338**, 277
- Rajpaul, V., Aigrain, S., Osborne, M. A., & Roberts, S. J. 2015, *MNRAS*, **452**, 2269
- Rogers, L. A. 2015, *ApJ*, **801**, 41
- Rogers, L. A., Bodenheimer, P., Lissauer, J. J., & Seager, S. 2011, *ApJ*, **738**, 59
- Rogers, L. A., & Seager, S. 2010a, *ApJ*, **712**, 974
- Rogers, L. A., & Seager, S. 2010b, *ApJ*, **716**, 1208
- Rowe, J. F., Bryson, S. T., Marcy, G. W., et al. 2014, *ApJ*, **784**, 45
- Schmitt, J. R., Agol, E., Deck, K. M., et al. 2014, *ApJ*, **795**, 167
- Schwarz, G. 1978, *AnSta*, **6**, 461
- Seager, S., Kuchner, M., HierMajumder, C. a., & Militzer, B. 2007, *ApJ*, **669**, 1279
- Vanderburg, A., Montet, B. T., Johnson, J. A., et al. 2015, *ApJ*, **800**, 59
- Weiss, L. M., & Marcy, G. W. 2014, *ApJL*, **783**, L6
- Wolfgang, A., & Lopez, E. 2015, *ApJ*, **806**, 183